Investigation on part-load performances of combined cooling and power system primed by solid oxide fuel cell with different bottoming cycles

X.J. Luo[1], K.F. Fong[2,*]

[1]Big Data Enterprise and Artificial Intelligence Laboratory, University of the West of England

[2]Division of Building Science and Technology, College of Engineering, City University of Hong Kong

*Corresponding author

Email address: bssquare@cityu.edu.hk

Postal address: Tat Chee Avenue, Kowloon, Hong Kong, China

Abstract

In hot-humid cities, conventional trigeneration can be reduced to combined cooling and power system. Solid oxide fuel cell is a high-temperature prime mover with high electrical efficiency, its efficiency may be further boosted up with bottoming cycle like gas turbine, Stirling engine and organic Rankine cycle. Besides using waste heat recovered from the prime mover to energize absorption chiller, the surplus electricity can be used to drive the conventional compression chiller as supplement. However, there is little knowledge about the effectiveness of such combined cooling and power system under different operating conditions. System models with various bottoming cycles are therefore developed, and their part-load performances are investigated. The effects of fuel inlet temperature and current density of fuel cell stack; compression ratio of gas turbine; Stirling engine type; working fluid of organic Rankine cycle; and fuel cell stack part-load ratio are explored. It is found that the combined cooling and power system with bottoming cycles of gas turbine and Stirling engine have higher boost of electrical efficiency. Gas turbine bottoming cycle is recommended when building energy demands are relatively constant, while Stirling engine bottoming cycle is suggested for variable energy

demands.

Keywords: Solid oxide fuel cell; bottoming cycle; gas turbine; Stirling engine; organic Rankine cycle; combined cooling and power.

1. Introduction

Combined cooling, heating and power (CCHP) systems have been widely used in buildings to furnish cooling, heating and electricity simultaneously. In CCHP systems, fuel is fed to the prime mover to generate electricity. Meanwhile, the by-product heat is recovered for heating and cooling purposes. Due to the possible primary energy saving of CCHP against the separate systems of heating and cooling, the overall energy efficiency could be improved and the carbon dioxide emissions would be reduced accordingly. In tropical and subtropical areas, space heating is generally not needed but there exists high cooling demand. Therefore, the CCHP system can be refined as combined cooling and power (CCP) system, thus the thermal energy from the prime mover can be fully utilized for cooling production. Solid oxide fuel cell (SOFC) stack is a promising high-temperature electrochemical conversion device for electricity generation due to its high electrical efficiency, fuel flexibility and low emissions [1,2]. The high operating temperature of SOFC stack enables the production of different grades of waste heat that can be recovered for power augmentation via gas turbine (GT), Stirling engine (SE) or organic Rankine cycle (ORC), to form the SOFC-GT, SOFC-SE or SOFC-ORC prime mover set. If the temperature of the exhaust gas is still high, it can be further utilized to drive the absorption chiller for cooling purpose. Meanwhile, due to the high electrical efficiency of SOFC stack, compression chiller can be added to supplement cooling production. As a result, the SOFC stack, integrated with various common bottoming cycles, can be regarded as effective prime mover sets for CCP systems.

The performances of SOFC-GT power generation systems were assessed in different occasions. Calise *et al*. [3] conducted exergy analysis of the SOFC-GT power generation system and it was

found that the SOFC stack had the largest exergy reduction. Zhao *et al*. [4] performed parametric analysis on various design parameters (i.e current density, operating temperature, fuel utilization and temperature gradient of the SOFC; isentropic efficiency and temperature ratio of GT) of the SOFC-GT power generation system to obtain higher electrical efficiency. Selimovic *et al.* [5] introduced the networked SOFC-GT power generation system to improve its electrical efficiency and reactant utilization. Chinda and Brault [6] evaluated the effects of different SOFC operating temperatures on the overall efficiency of SOFC-GT power generation system. Cheng *et al.* [7] conducted an exergoeconomic analysis of the SOFC-GT power generation system and demonstrated its improvement in high electrical efficiency and low environmental cost. Jia *et al.* [8] carried out an energy and techno-economic assessment of a SOFC-GT power generation system which was based on co-gasification of woody biomass and animal manure. Various thermodynamic models of SOFC-GT hybrid power system were also developed in [9-14] and it was concluded that its electrical efficiency was between 50% and 70%. Tse *et al.* [15] investigated the feasibility of combining the SOFC-GT set and an absorption chiller in the CCHP system. They developed the mathematical models of SOFC stack and GT based on the measurement data. Meanwhile, the pressure ratio of GT, gas inlet temperature of GT and current density of SOFC stack were fixed at certain values. In [16-18], optimal operating parameters of the SOFC-GT-primed combined heating and power (CHP) system were chosen through evolutionary algorithms to maximize the exergy efficiency and minimize system cost under different electrical power requirements. Burer *et al.* [19] conducted a thermo-economical optimization of an SOFC-GT-primed CCHP system to minimize its annual cost and CO_2 emissions. However, since the focus of these studies was performance evaluation and parameter optimization at the design stage, simplified mathematical models were adopted to simulate the full-load operating performance of GT. For instance, constant isentropic efficiency of GT was assumed in [3-5,8,16-19]; typical GT maps were generated by simulation program GSP or GasTurb in [6,9,10,12,13]; the GT map of a specific axial turbine was adopted in [9]; the GT map was constructed using the experimental results in [14,15]. These GT models were case-specific in general.

Compared to hybrid SOFC-GT systems, research works regarding SOFC-SE and SOFC-ORC sets were fewer. Chen *et al.* [20] investigated the feasibility of a SOFC-SE power generation system during full-load operation at design condition. In [21, 22], the effects of SOFC inlet temperature and current density, along with the compression ratio and regenerator effectiveness of SE, on the electrical efficiency of the SOFC-SE power generation system were investigated. Rokni [23-26] built the thermodynamic models of the SOFC-SE-primed CHP system and evaluated its thermo-economic performance at full-load operating condition. In addition to the SOFC-SE power generation set, domestic hot water was used as the heat sink for the SE to further utilize its thermal energy. In [25], the effects of fuel utilization factor, oxygen-to-carbon ratio and fuel preheating temperature on the electrical efficiency of the SOFC-SE-primed CHP system were evaluated. In [26], system efficiency at different fuels (i.e. natural gas, ammonia, dimethyl ether, methanol and ethanol) was evaluated. Habibollahzade *et al*. [27] evaluated the thermodynamic, environmental and economic feasibility of the SOFC-SE power generation system was evaluated. Since the main purpose of these research works was the feasibility assessment, simplified SE models were generally used. Like [20,22], finite-time thermodynamic model of SE was adopted, and it was assumed that the operating time spent on the regenerative branches was proportional to that of the isothermal branches. In [21,23-26], pseudo SE model was adopted. In the finite-time thermodynamic and pseudo model, various efficiencies affecting the overall performance of SE were not considered.

Kalina *et al.* [28] evaluated the energy and economic performance of a biomass-based SOFC-ORC power generation system. Ebrahimi *et al.* [29] investigated the various design parameters of SOFC (i.e. current density, fuel flow rate, steam to carbon ratio, heat loss, fuel utilization factor, operating temperature and pressure) on the electrical efficiency of the hybrid power generation system consisting of SOFC, GT and ORC. In [30,31], the effects of SOFC design parameters (i.e. current density, compressor pressure ratio, fuel utilization and SOFC temperature) and ORC design parameters (i.e. turbine inlet pressure and condenser temperature) on the electrical efficiency of the SOFC-ORC hybrid power system were explored. Al-Sulaiman *et al.* [32,33] conducted energy and exergy analysis of SOFC-ORC-primed CCHP system. Absorption chiller was adopted to convert the

recovered thermal energy from SOFC-ORC set to cooling energy. It was found that the system efficiency increased 22% compared with the SOFC-ORC power generation system. And the maximum system efficiency obtained from the CCHP system was 74% at full-load operation. Amicabile *et al*. [34] demonstrated the feasibility of using ORC to recover the heat from the reversible SOFC stack to improve the total electrical efficiency of the SOFC-ORC power generation system. Ghaffarpour *et al*. [35] carried out thermo-economic analysis and multi-objective optimization on a hybrid power generation system consisting of SOFC stack, GT and a Rankine cycle. Owebor *et al.* [36] demonstrated the technical, economic and environmental feasibility and sustainability of a hybrid power generation system using SOFC stack, GT and ORC. Since the main purpose of the above-mentioned studies about ORC was the evaluation of full-load operation at design stage, isentropic efficiency of its turbine was assumed constant.

From the above literature review, previous research works regarding SOFC-GT/SE/ORC-primed CHP/CCHP system mainly focused on performance evaluation and parameter optimization at the design stage and full-load operation. The lumped model of SOFC stack was adopted while the temperatures of the outlet fuel and air flows were generally assumed the same and constant. As a result, it is necessary to conduct a comprehensive analysis of SOFC with common bottoming cycles based on the following gaps of research:

- There was no previous study discussing the configuration and performance of CCP system primed by SOFC with various bottoming cycles.
- Part-load performance of the SOFC, GT, SE and ORC were commonly overlooked in performance assessment.
- For cooling production, absorption chiller (AbC) was adopted to utilize the thermal energy recovered from prime mover set of SOFC-bottoming cycle, while the compression chiller (CoC) with better coefficient of performance was not considered.
- Electrical efficiency was commonly chosen as the assessment criterion in the previous study, while the effectiveness of the system in satisfying variable cooling, heating and electricity demand was not explored.
- None of the existing works considered about recovering the thermal energy from the condenser of the ORC for additional cooling production.

The objective of study is to systematically investigate the effects of key parameters and part-load operation on the efficiencies and effectiveness of SOFC-GT/SE/ORC-primed CCP systems. A comprehensive two-dimensional dynamic model was employed to simulate both electrochemical and thermodynamic performance of the SOFC stack. In the SOFC model, electrochemical reaction, chemical reaction, flow field, mass transfer and energy transfer sub-models were coupled to determine its distribution of current density, temperature, pressure and gas composition. Moreover, part-load operating performance was considered in the GT, SE and ORC thermodynamic models. Apart from absorption chiller, compression chiller was also adopted due to the high electrical efficiency of the SOFC prime mover set. Meanwhile, a new performance index was introduced to evaluate the effectiveness of the proposed SOFC-GT/SE/ORC CCP systems. The effects of various critical parameters including current density and fuel inlet temperature of SOFC stack, compression ratio of GT, type of SE and working fluid of ORC on both system efficiency and effectiveness were evaluated.

This paper is structured in the following way. Section 2 describes the configurations and operating principles of the SOFC-primed CCP reference system, the SOFC-GT-primed CCP system, the SOFC-SE-primed CCP system and the SOFC-ORC-primed CCP system. Section 3 depicts the mathematical models of key equipment units in CCP systems primed by SOFC with different bottoming cycles. Section 4 introduces the performance assessment criteria, including electrical efficiency, overall efficiency and a performance index defined to evaluate the effectiveness of the CCP systems. Section 5 analyses and discusses the performance results of various CCP systems. Section 6 presents the conclusion of this study and gives suggestions for system design and selection. Appendix A covers the thermodynamic models other than the essential ones, while Appendix B consolidates the thermodynamic properties of fluid flow in each CCP system.

2. Configurations of CCP system primed by SOFC with different bottoming cycles

In this research, three new configurations of CCP systems were developed, which were driven by SOFC stack and designed with the common bottoming cycles (i.e. GT, SE and ORC). Meanwhile, the SOFC-primed CCP system was built as comparison reference. The schematic design of the SOFC-

primed CCP reference system, the SOFC-GT-primed CCP system, the SOFC-SE-primed CCP system and the SOFC-ORC-primed CCP system are shown in Fig. 1.

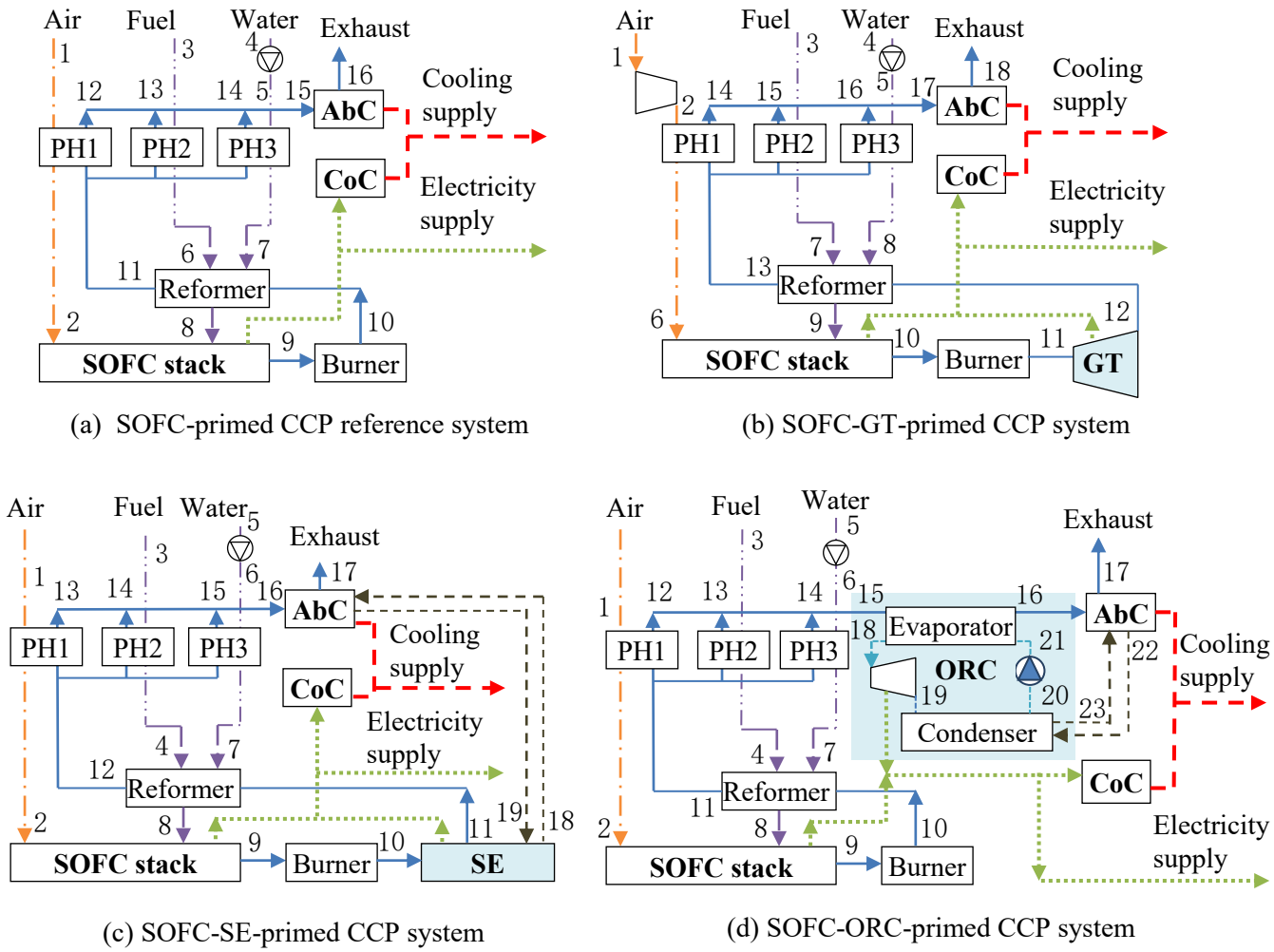

(a) SOFC-primed CCP reference system

(b) SOFC-GT-primed CCP system

(c) SOFC-SE-primed CCP system

(d) SOFC-ORC-primed CCP system

Fig. 1. Schematic design of the four SOFC-primed CCP systems investigated

As shown in Fig. 1(a), in the SOFC-primed CCP reference system, the pre-heated fuel (i.e. methane) and water were delivered to the reformer. In the reformer, 30% of methane was pre-reformed. The gas mixture from the reformer then reacted electrochemically with the preheated air in the SOFC stack to generate electricity. The SOFC stack operated at ambient pressure. After that, the unreacted fuel from the SOFC stack was combusted in the burner and further used to supply heat for the reformer and the three pre-heaters. Then, it would be delivered to energize the absorption chiller (AbC). Due to the high electrical efficiency of the SOFC stack and high cooling demand in building, the compression chiller (CoC) was also involved to supplement the total cooling capacity.

Fig. 1(b) shows the configuration of the SOFC-GT-primed CCP system. According to the original system configuration of GT [37], fuel was directly injected for combustion, while air needed to be compressed before delivered to the pre-heater and the SOFC stack. Thus, the operating pressure of the SOFC stack was higher than that in the SOFC-primed CCP reference system. The higher operating pressure would also help increase the cell voltage and the electrical efficiency of the SOFC stack. The pressured exhaust gas from the burner was then expanded in the GT to generate additional electricity.

The configuration of the SOFC-SE-primed CCP system is illustrated in Fig. 1(c). The high-temperature exhaust gas from the burner was used as heat source for the SE before delivered to reformer and three pre-heaters. Meanwhile, the AbC was used as the heat sink for the SE to further utilize its thermal energy.

Fig. 1(d) describes the energy and fluid flow of the SOFC-ORC-primed CCP system. Since the critical temperature of the working fluid in ORC is lower than 600 K, the required temperature of heat source for ORC was lower than that of GT and SE. Before providing thermal energy for the ORC through the evaporator, the exhaust gas of burner was delivered to the reformer and three pre-heaters. In this study, two types of ORC were studied. In A-type, the condenser temperature was designed at 400 K, thus it could be further used to energize the AbC and increase cooling production. In B-type, the condenser temperature was designed at 300 K, thus the electrical efficiency of ORC could be improved.

3. Development of system models for various CCP systems

In order to evaluate the system performance under different operating and loading conditions, part-load performance in key equipment units including SOFC stack, GT, SE and ORC were developed.

Lumped models were adopted for pre-heaters, reformer, burner, absorption chiller and compression chiller, which are covered in Appendix A.

3.1 SOFC stack

In order to accurately simulate the temperature of the fluid flow in the fuel and air channel, the two-dimensional dynamic model of the SOFC unit proposed in our previous research was used [38-40]. In the SOFC model, the electrochemical reaction, mass transfer, momentum transfer and heat transfer sub-models were fully coupled.

3.1.1 Electrochemical reaction sub-model

$$U = U_{oc} - U_{act,an} - U_{act,ca} - U_{conc,an} - U_{conc,ca} - U_{ohm} \tag{1}$$

$$U_{oc} = -\frac{\Delta h_{T,p0} - T\Delta s_{T,p0}}{2F} + \frac{RT}{2F} ln\left[\frac{p_{H_2,fc}\, p_{O_2,ac}^{\frac{1}{2}}}{p_{H_2O,ac}\, p_0^{\frac{1}{2}}}\right] \tag{2}$$

$$U_{act,an} = \frac{RT}{F} ln\left[\frac{J}{2J_{ex,an}} + \sqrt{\left(\frac{J}{2J_{ex,an}}\right)^2 + 1}\right] \tag{3}$$

$$U_{act,ca} = \frac{RT}{F} ln\left[\frac{J}{2J_{ex,ca}} + \sqrt{\left(\frac{J}{2J_{ex,ca}}\right)^2 + 1}\right] \tag{4}$$

$$U_{conc,an} = \frac{RT}{2F} ln\left[\frac{p_{H_2,fc}\; p_{H_2O,an-ely}}{p_{H_2,an-ely}\; p_{H_2O,fc}}\right] \tag{5}$$

$$U_{conc,ca} = \frac{RT}{2F} ln\left[\frac{p_{O_2,ac}}{p_{O_2,ca-ely}}\right] \tag{6}$$

$$U_{ohm} = J\left[d_{an}\frac{T}{9.5\times10^7\cdot exp(-\frac{1150}{T})} + + d_{ele}\frac{1}{3.34\times10^4\cdot exp(-\frac{10300}{T})} + d_{ca}\frac{T}{4.2\times10^7\cdot exp(-\frac{1200}{T})}\right] \tag{7}$$

$$P_{SOFC} = 3.6\ UJA \tag{8}$$

where,

U: voltage of SOFC unit (V)

U_{oc}: open circuit voltage (V)

$U_{act,an}$: activation overpotential at the anode (V)

$U_{act,ca}$: activation overpotential at the cathode (V)

$U_{conc,an}$: concentration overpotential at the anode (V)

$U_{conc,ca}$: concentration overpotential at the cathode (V)

U_{ohm}: total ohmic overpotential of the anode, electrolyte and cathode (V)

J: current density (A/m^2)

T: temperature (K)

p: pressure (Pa)

d: thickness (m)

F: Faraday constant, and F = 96,485 ($A \cdot s \cdot mol^{-1}$)

R: Gas constant (8.314 $m^3 \cdot Pa \cdot K^{-1} mol^{-1}$)

P: electrical power output of SOFC unit (kJ/h)

A: total surface area of SOFC stack (m^2)

3.1.2 Mass transfer sub-model

$$\frac{\partial \rho u}{\partial x} + \frac{\partial \rho v}{\partial z} = S_{mt} \tag{9}$$

$$\frac{\partial \rho u Y_{mi}}{\partial x} + \frac{\partial \rho v Y_{mi}}{\partial z} = \frac{\partial}{\partial x}\sigma \frac{\partial \rho Y_{mi}}{\partial x} + \frac{\partial}{\partial z}\sigma \frac{\partial \rho Y_{mi}}{\partial z} + S_{mi} \tag{10}$$

where,

ρ: density of the gas mixture ($kg \cdot m^{-3}$)

u, v: velocity vectors in the x and z directions, respectively ($m \cdot s^{-1}$)

S_{mt}, S_{mi}: total and gas species volumetric mass source rate resulting from chemical and electrochemical reactions ($kg \cdot m^{-3} s^{-1}$)

Y: mass fraction of each gas species

σ: effective diffusion coefficient of each gas species ($m^2 \cdot s^{-1}$)

3.1.3 Momentum transfer sub-model

$$\frac{\partial(\rho u)}{\partial t}+\frac{\partial(\rho u u)}{\partial x}+\frac{\partial(\rho v u)}{\partial z}=\frac{\partial P}{\partial x}+\frac{\partial}{\partial x}\left(\mu\frac{\partial u}{\partial x}\right)+\frac{\partial}{\partial z}\left(\mu\frac{\partial u}{\partial z}\right)+S_{mu} \tag{11}$$

$$\frac{\partial(\rho v)}{\partial t}+\frac{\partial(\rho u v)}{\partial x}+\frac{\partial(\rho v v)}{\partial z}=\frac{\partial P}{\partial z}+\frac{\partial}{\partial x}\left(\mu\frac{\partial v}{\partial x}\right)+\frac{\partial}{\partial z}\left(\mu\frac{\partial v}{\partial z}\right)+S_{mv} \tag{12}$$

where,

S_{mu}, S_{mv}: the momentum source at x and z direction, respectively ($kg \cdot m^{-2}s^{-2}$).

3.1.4 Heat transfer sub-model

$$\frac{\partial(\rho C_p\, T)}{\partial t}+\frac{\partial(\rho C_p\, uT)}{\partial x}+\frac{\partial(\rho C_p\, vT)}{\partial z}=\frac{\partial}{\partial x}(k\frac{\partial T}{\partial x})+\frac{\partial}{\partial z}(k\frac{\partial T}{\partial z})+S_q \tag{13}$$

where,

C_p: specific heat ($J \cdot kg^{-1}K^{-1}$)

k: thermal conductivity ($W \cdot K^{-1}m^{-1}$)

S: volumetric heat source rate resulting from the Joule heating and reaction heats of the chemical and electrochemical reactions ($J \cdot m^{-3}s^{-1}$)

To generate practical electrical power output, the SOFC stack was made up of a number of SOFC units connected in series and/or parallel. To maintain the high electrical efficiency at part-load operation, the SOFC stack was equally divided into 10 sub-stacks. When the required electrical power output was lower than the design capacity of the SOFC-GT set, fewer SOFC sub-stacks would operate. In this connection, part-load ratio of the SOFC stack *PLR* was defined as the ratio of operating quantity of SOFC sub-stacks at part-load operation $N_{SOFC,pl}$ to the total quantity of SOFC sub-stacks $N_{SOFC,fl}$, thus:

$$N_{SOFC,pl} = PLR \times N_{SOFC,fl} \tag{14}$$

In practical application, the fuel and air inlets are distributed on each SOFC sub-stack. By supplying adequate amount of fuel and air to the operating SOFC sub-stacks, its part-load ratio can be adjusted.

To make it consistent, in the following study, the *PLR* of SOFC-GT-, SOFC-SE- and SOFC-ORC-primed CCP systems was also defined by Eq. (9). The design capacity of SOFC stack equaled to the total electrical power output of the SOFC unit, thus:

$$C_{SOFC} = P_{SOFC} \tag{15}$$

3.2 Gas turbine

Based on the SOFC-primed CCP reference system, the air compressor and GT were involved to constitute the SOFC-GT-primed CCP system, as shown in Fig. 1(b). Thermodynamic models of the GT and air compressor were developed based on [41]:

$$T_{GT,out,is} = T_{GT,in}\,\pi_{GT}^{(\kappa-1)/\kappa} \tag{16}$$

$$\gamma_{GT} = (h_{GT,in} - h_{GT,out})/(h_{GT,in} - h_{GT,out,is}) \tag{17}$$

$$T_{com,out,is} = T_{com,in}\,\pi_{com}^{(\kappa-1)/\kappa} \tag{18}$$

$$\gamma_{com} = (h_{com,in} - h_{com,out})/(h_{com,in} - h_{com,out,is}) \tag{19}$$

where,

$T_{GT,out,is}$ and $T_{com,out,is}$: fluid flow isentropic outlet temperature of GT and air compressor (K)

$h_{GT,out,is}$ and $h_{com,out,is}$: fluid flow isentropic specific enthalpy of GT and air compressor (kJ·kg^{-1})

$h_{GT,in}$ and $h_{GT,out}$: specific enthalpy of inlet and outlet fluid flow of GT (kJ·kg^{-1})

$h_{com,in}$ and $h_{com,out}$: specific enthalpy of inlet and outlet fluid flow of air compressor (kJ·kg^{-1})

κ: specific heat ratio of fluid flow

π_{GT} and π_{com}: compression ratio of GT and air compressor

η_{GT} and η_{com}: isentropic efficiency of GT and air compressor

The electrical power output of GT P_{GT} (kJ·h^{-1}) and the electrical power consumption of compressor P_{com} (kJ·h^{-1}) were determined by the enthalpy difference and its mechanical efficiency:

$$P_{GT} = m_{exh}(h_{GT,in} - h_{GT,out})\eta_{mech,GT} \quad (20)$$

$$P_{com} = m_{exh}\,(h_{com,out} - h_{com,in})/\eta_{mech,com} \quad (21)$$

where,

$\eta_{mech,GT}$ and $\eta_{mech,com}$: mechanical efficiency of GT and air compressor (%)

m_{exh}: mass flow rate of exhaust gas (kg·h^{-1})

The design capacity of the GT $C_{GT,S1}$ in the SOFC-GT-primed CCP system was defined as the net electrical power generated by the GT P_{GT} minus power consumption of the air compressor P_{com}:

$$C_{GT,S1} = P_{GT} - P_{com} \quad (22)$$

As rotational components, the performance of air compressor and GT was largely affected by the inlet flow rate of fluid flow. Since the mass flow rate of air m_a was much larger than that of methane m_m, keeping m_a constant would ensure a relatively stable performance of both air compressor and GT. Thus, the air compressor would be used to operate at full-load condition. The inlet mass flow rates of methane and water were adjusted based on the *PLR* of the SOFC-GT-primed CCP system as follows:

$$m_{m,pl} = PLR\ m_{m,fl} \quad (23)$$

$$m_{w,pl} = PLR\ m_{w,fl} \quad (24)$$

where,

$m_{m,pl}$ and $m_{w,pl}$: inlet mass flow rates of methane and water at part-load operation (kg·h^{-1})

$m_{m,fl}$ and $m_{w,fl}$: inlet mass flow rates of methane and water at full-load operation (kg·h^{-1})

At part load operation, the isentropic efficiency and compression ratio of GT was determined using

the following mathematical expressions:

$$B_I = \frac{\eta_{GT,pl}}{\eta_{GT,fl}} = (\frac{1}{B_{II}})(2 - \frac{1}{B_{III}}) \quad (25)$$

$$B_{II} = \frac{m_{GT,pl}\sqrt{T_{GT,pl,in}}}{m_{GT,fl}\sqrt{T_{GT,fl,in}}} \quad (26)$$

$$B_{III} = \sqrt{\frac{T_{GT,fl,in}}{T_{GT,pl,in}}}\sqrt{\frac{\pi_{GT,pl}^2 - 1}{\pi_{GT,fl}^2 - 1}} \quad (27)$$

3.3 Stirling engine

Finite speed thermodynamic analysis was used to develop the model of SE in order to take various pressure loss into account [42]. The power output of the SE was affected by the efficiencies of thermodynamic cycle η_{cycle}, regenerator η_{reg} and pressure loss $\eta_{\Delta p}$:

$$P_{SE} = \eta_{cycle}\ \eta_{reg}\ \eta_{\Delta p}\ Q_{SE} \quad (28)$$

$$\eta_{cycle} = 1 - \frac{T_L + \Delta T_L}{T_H - \Delta T_H} \quad (29)$$

$$\eta_{reg} = \frac{1}{1 + \frac{(1-\varepsilon reg)\eta_{cycle}}{(\kappa - 1)\ ln\ \pi_{SE}}} \quad (30)$$

$$\eta_{\Delta P} = 1 - \frac{\left(3 - \frac{1}{r}\right)\Sigma\frac{\Delta p(r+1)(\frac{T_H - \Delta T_H}{T_L + \Delta T_L} + 1)}{4p_{SE}}}{\eta_{cycle}\eta_{re}\left(\frac{T_H - \Delta T_H}{T_L + \Delta T_L}\right) ln\ \pi_{SE}} \quad (31)$$

where,

T_L and T_H: temperature of cold sink and hot source (K)

ε_{reg}: effectiveness of regenerator

Q_{SE}: the recovered thermal energy which was used to drive SE (kJ·h^{-1})

π_{SE}: compression ratio of SE.

In this study, three types of SE (i.e. α, β and γ) were analyzed, and the corresponding π_{SE} were determined as follows:

$$\pi_{\alpha-SE} = 1 + \frac{2\sqrt{1+\left(\frac{V_{SE,s,c}}{V_{SE,s,e}}\right)^2}}{2\left(\frac{V_{SE,d}}{V_{SE,s,e}}\right)+1+\left(\frac{V_{SE,s,c}}{V_{SE,s,e}}\right)-\sqrt{1+\left(\frac{V_{SE,s,c}}{V_{SE,s,e}}\right)^2}} \quad (32)$$

$$\pi_{\beta-SE} = 1 + \frac{2\left(\frac{V_{SE,s,c}}{V_{SE,s,e}}\right)}{2\left(\frac{V_{SE,d}}{V_{SE,s,e}}\right)+1-\left(\frac{V_{SE,s,c}}{V_{SE,s,e}}\right)+\sqrt{1+\left(\frac{V_{SE,s,c}}{V_{SE,s,e}}\right)^2}} \quad (33)$$

$$\pi_{\gamma-SE} = 1 + \frac{\left(\frac{V_{SE,s,c}}{V_{SE,s,e}}\right)}{1+\left(\frac{V_{SE,d}}{V_{SE,s,e}}\right)} \quad (34)$$

where,

$V_{SE,s,c}$: swept volume of compression (m^3)

$V_{SE,s,e}$: swept volume of expansion (m^3)

$V_{SE,d}$: dead volume (m^3)

The pressure in SE was described as:

$$p_{SE} = m_{he}R / (V_{SE,c}/T_{SE,c} + V_{SE,co}/T_{SE,co} + V_{SE,reg}/T_{SE,reg} + V_{SE,he}/T_{SE,he} + V_{SE,e}/T_{SE,e}) \quad (35)$$

where,

m_{he}: mass of helium in SE (kg)

$V_{SE,c}$, $V_{SE,co}$, $V_{SE,reg}$, $V_{SE,he}$, $V_{SE,e}$: volume of compression, cooler, regenerator, heater and expansion in SE (m^3)

$T_{SE,c}$, $T_{SE,co}$, $T_{SE,reg}$, $T_{SE,he}$, $T_{SE,e}$: temperature of compression, cooler, regenerator, heater and expansion in SE (K)

The design capacity of SE $C_{SE,S2}$ equaled to net electrical power generated by SE:

$$C_{SE,S2} = P_{SE} \tag{36}$$

3.4 Organic Rankine cycle

As shown in Fig. 1(d), the working fluid absorbed heat in the evaporator and converted it into electrical power through the ORC turbine. The developed models of the SOFC-ORC-primed CCP system are described below.

3.4.1 Evaporator

$$m_{wf,ORC}\,(h_{18} - h_{17}) = m_{exh}\,(h_{14} - h_{15}) \tag{37}$$

where,

$m_{wf,ORC}$ and m_{exh}: mass flow rate of working fluid in ORC and exhaust gas, respectively ($kg \cdot h^{-1}$)

3.4.2 ORC turbine

The mathematical model of ORC turbine was similar to that of the GT described in Section 3.2. Thus the electrical power generated by ORC turbine $P_{ORC,tur}$ and electrical power consumed in the ORC pump $P_{ORC,pump}$ can be calculated as [43]:

$$P_{ORC,tur} = m_{wf,ORC}\,(h_{18} - h_{19}) \tag{38}$$

$$P_{ORC,pump} = m_{ORC}\,(h_{21} - h_{20}) \tag{39}$$

The design capacity of the ORC C_{ORC} was defined as the net electrical power generated by the ORC turbine minus power consumption of ORC pump:

$$C_{ORC} = P_{ORC,tur} - P_{ORC,pump} \quad (40)$$

3.4.3 Condenser

In A-type SOFC-ORC-primed CCP system, the condenser was maintained at 400 K, thus it could provide heat for the AbC. The thermal energy provided by the condenser Q_{con} was calculated as:

$$Q_{con} = m_{wf,ORC}\,(h_{19} - h_{20}) \quad (41)$$

3.5 Design parameters of various CCP systems

The design parameters of the SOFC-primed CCP reference system, the SOFC-GT-primed CCP system, the SOFC-SE-primed CCP system and the SOFC-ORC-primed CCP system are summarized in Table 1.

Table 1. Operating parameters of different CCP systems.

Common parameters of different CCP systems [38, 39]	**Value**
SOFC inlet temperature (K)	[923, 973, 1023, 1073, 1123]
Current density (A/m^2)	[4000, 5000, 6000, 7000, 8000]
Fuel utilization ratio of SOFC	0.85
Air excess ratio of SOFC	2
Effectiveness of pre-heaters (%)	80
Efficiency of reformer (%)	90
Efficiency of burner (%)	98
Efficiency of pump (%)	98
Temperature of hot water for AbC (K)	363
COP of AbC	0.7
COP of CoC	5
Parameters of SOFC-GT-primed CCP system [19]	
Compression ratio of air/methane compressor	[2, 2.5, 3, 3.5, 4]
Isentropic efficiency of air compressor (%)	90
Mechanical efficiency of air compressor (%)	98
Isentropic efficiency of GT (%)	85
Mechanical efficiency of GT (%)	98
Parameters of SOFC-SE-primed CCP system [23]	
Swept volume of compression ($\times 10^{-9}$ m^3)	120.8
Dead volume of compression ($\times 10^{-9}$ m^3)	28.7
Swept volume of expansion ($\times 10^{-9}$ m^3)	113.1
Dead volume of expansion ($\times 10^{-9}$ m^3)	30.5
Volume of regenerator ($\times 10^{-9}$ m^3)	50.55
Volume of heater ($\times 10^{-9}$ m^3)	70.88
Volume of cooler ($\times 10^{-9}$ m^3)	13.8
Effectiveness of regenerator (%)	80
Regenerator diameter ($\times 10^{-3}$ m)	22.6
Number of gauzes of the matrix in the regenerator	300
Piston diameter ($\times 10^{-3}$ m)	22.2
Stroke (m)	0.0312
Frequency (Hz)	41.7
Parameters of SOFC-ORC-primed CCP system [32]	
Isentropic efficiency of ORC turbine (%)	85
Isentropic efficiency of ORC pump (%)	90
Effectiveness of the ORC evaporator (%)	80
Pressure of ORC evaporator ($\times 10^5$ Pa)	30
Temperature of condenser (K)	A-type, 300 for B-type

4. Criteria of performance assessment

To facilitate assessing the efficiency and effectiveness of each CCP system, the contribution ratios in each CCP systems were defined. After that, the definitions of electrical efficiency, overall efficiency,

and electrical efficiency boost, as well as performance index for evaluating system effectiveness, were illustrated.

4.1 Contribution ratio

For the SOFC-primed reference CCP system, at certain fuel inlet temperature $T_{f,in}$ and part-load ratio *PLR*, there existed a contribution ratio ξ_{S0} between cooling capacity of AbC $C_{AbC,S0}$ and electrical power output of $C_{SOFC,S0}$ as follows:

$$\xi_{S0} = C_{AbC,S0}/C_{SOFC,S0} \tag{42}$$

In the SOFC-GT-primed CCP system, the SOFC-SE-primed CCP system and the SOFC-ORC-primed CCP systems, once the design capacity of SOFC stack was determined, the capacity of GT $C_{GT,S1}$, the capacity of SE $C_{SE,S2}$, the capacity of A-type ORC $C_{ORC,S3,A}$, the capacity of B-type ORC $C_{ORC,S3,B}$, as well as the capacity of AbC in each CCP system (i.e. $C_{AbC,S1}$, $C_{AbC,S2}$, $C_{AbC,S3,A}$, $C_{AbC,S3,B}$), could be decided. Thus, the contribution ratios in each CCP system were defined, with $\xi_{S1,E}$, $\xi_{S2,E}$, $\xi_{S3,A,E}$ and $\xi_{S3,B,E}$ indicating the ratio of electricity capacity of bottoming cycles to that of the SOFC stack, while $\xi_{S1,C}$, $\xi_{S2,C}$, $\xi_{S3,A,C}$ and $\xi_{S3,B,C}$ standing for the ratio of cooling capacity of AbC to the electricity capacity of SOFC as follows:

$$\xi_{S1,E} = C_{GT,S1}/C_{SOFC,S1} \tag{43}$$

$$\xi_{S1,C} = C_{AbC,S1}/C_{SOFC,S1} \tag{44}$$

$$\xi_{S2,E} = C_{SE,S2}/C_{SOFC,S2} \tag{45}$$

$$\xi_{S2,C} = C_{AbC,S2}/C_{SOFC,S2} \tag{46}$$

$$\xi_{S3,A,E} = C_{ORC,S3,A}/C_{SOFC,S3,A} \tag{47}$$

$$\xi_{S3,A,C} = C_{AbC,S3,A}/C_{SOFC,S3,A} \tag{48}$$

$$\xi_{S3,B,E} = C_{ORC,S3,B}/C_{SOFC,S3,B} \tag{49}$$

$$\xi_{S3,B,C} = C_{AbC,S3,B}/C_{SOFC,S3,B} \tag{50}$$

When fuel inlet temperature of SOFC stack is the same in using certain type of working fluid, $\xi_{S3,A,E}$ would be smaller than $\xi_{S3,B,E}$, while $\xi_{S3,A,C}$ would be larger than $\xi_{S3,B,C}$. Because in A-type SOFC-ORC-primed CCP system, the temperature difference between evaporator and condenser was smaller, while the thermal energy in the condenser was recovered for AbC due to higher operating temperature of the condenser.

4.2 Electrical efficiency, overall efficiency and electrical efficiency boost

In SOFC-primed CCP reference system, SOFC-GT-primed CCP system, SOFC-SE-primed CCP system and SOFC-ORC-primed CCP system (A-type and B-type), the electrical power was generated by SOFC stack, SOFC-GT set, SOFC-SE set and SOFC-ORC set, respectively. Thus, the electrical efficiencies of the corresponding CCP systems were calculated as follows:

$$\eta_{S0,ele} = C_{SOFC,S0}/(n_{CH4,in}\, LHV_{CH4,in}) \tag{51}$$

$$\eta_{S1,ele} = (C_{SOFC,S1} + C_{GT,S1})/(n_{CH4,in}\, LHV_{CH4,in}) \tag{52}$$

$$\eta_{S2,ele} = (C_{SOFC,S2} + C_{SE,S2})/(n_{CH4,in}\, LHV_{CH4,in}) \tag{53}$$

$$\eta_{S3,A,ele} = (C_{SOFC,S3,A} + C_{ORC,S3,A})/(n_{CH4,in}\, LHV_{CH4,in}) \tag{54}$$

$$\eta_{S3,B,ele} = (C_{SOFC,S3,B} + C_{ORC,S3,B})/(n_{CH4,in}\, LHV_{CH4,in}) \tag{55}$$

In order to understand the performance effect due to incorporating the bottoming cycle in the corresponding CCP system, the electrical efficiency boost was therefore introduced to compare against the SOFC-primed CCP reference system. The electrical efficiency boost of SOFC-GT-primed CCP system $\Delta\eta_{S1,ele}$, that of SOFC-SE-primed CCP system $\Delta\eta_{S2,ele}$, and that of SOFC-ORC-primed CCP system $\eta_{S3,A,ele}$ or $\eta_{S3,B,ele}$ could be obtained as follows:

$$\Delta\eta_{S1,ele} = \eta_{S1,ele} - \eta_{S0,ele} \tag{56}$$

$$\Delta\eta_{S2,ele} = \eta_{S2,ele} - \eta_{S0,ele} \tag{57}$$

$$\Delta\eta_{S3,A,ele} = \eta_{S3,A,ele} - \eta_{S0,ele} \quad (58)$$

$$\Delta\eta_{S3,B,ele} = \eta_{S3,B,ele} - \eta_{S0,ele} \quad (59)$$

And the overall efficiencies of the respective CCP systems were computed as follows:

$$\eta_{S0,overall} = (C_{SOFC,S0} + Q_{AbC,S0})/(n_{CH4,in}\, LHV_{CH4,in}) \quad (60)$$

$$\eta_{S1,overall} = (C_{SOFC,S1} + C_{GT,S1} + Q_{AbC,S1})/(n_{CH4,in}\, LHV_{CH4,in}) \quad (61)$$

$$\eta_{S2,overall} = (C_{SOFC,S2} + C_{SE,S2} + Q_{AbC,S2})/(n_{CH4,in}\, LHV_{CH4,in}) \quad (62)$$

$$\eta_{S3,A,overall} = (C_{SOFC,S3,A} + C_{ORC,S3,A} + Q_{AbC,S3,A})/(n_{CH4,in}\, LHV_{CH4,in}) \quad (63)$$

$$\eta_{S3,B,overall} = (C_{SOFC,S3,B} + C_{ORC,S3,B} + Q_{AbC,S3,B})/(n_{CH4,in}\, LHV_{CH4,in}) \quad (64)$$

4.3 Performance index

To facilitate performance evaluation, the design capacity of SOFC stack, AbC and CoC of the SOFC-primed CCP reference system was determined first. And it was based upon the condition that the SOFC-primed CCP reference system was sufficient to simultaneously satisfy both cooling demand D_C (kJ·h^{-1}) and electricity demand D_E (kJ·h^{-1}) of the building, as well as the power consumption of parasitic equipment units P_{para} (kJ·h^{-1}), as follows:

$$C_{SOFC,S0} = C_{CoC}/COP_{CoC} + D_E + P_{para} \quad (65)$$

$$C_{AbC,S0} + C_{CoC} = D_C \quad (66)$$

Thus,

$$C_{SOFC,S0} = \frac{D_C\left[1+\left(\frac{D_E+P_{para}}{D_C}\right)COP_{CoC}\right]}{(\xi_1+COP_{CoC})} \quad (67)$$

In SOFC-GT-, SOFC-SE- and SOFC-ORC-primed CCP systems, the design capacity of SOFC stack was set identical as the SOFC-primed CCP reference system. Assuming that the cooling demand D_C was equal to the total cooling capacity of AbC and CoC, while the electrical power generated by each system should not be less than electricity demand D_E. As such, the following expressions were set:

$$C_{AbC,S1} + C_{CoC} = D_C \tag{68}$$

$$C_{SOFC,S1} + C_{GT,S1} \geq C_{CoC}/COP_{CoC} + D_E + P_{para} \tag{69}$$

$$C_{AbC,S2} + C_{CoC} = D_C \tag{70}$$

$$C_{SOFC,S2} + C_{SE,S2} \geq \mathrm{C_{CoC}/COP_{CoC}} + D_E + P_{para} \tag{71}$$

$$C_{AbC,S3,A} + C_{CoC} = D_C \tag{72}$$

$$C_{SOFC,S3,A} + C_{ORC,S3,A} \geq C_{CoC}/COP_{CoC} + D_E + P_{para} \tag{73}$$

$$C_{AbC,S3,B} + C_{CoC} = D_C \tag{74}$$

$$C_{SOFC,S3,B} + C_{ORC,S3,B} \geq C_{CoC}/COP_{CoC} + D_E + P_{para} \tag{75}$$

By integrating Eqs. (42)-(50), the following relationships could be obtained:

$$\xi_{S1,E} + \xi_{S1,C}/COP_{CoC} \geq \xi_{S0}/COP_{CoC} \tag{76}$$

$$\xi_{S2,E} + \xi_{S2,C}/COP_{CoC} \geq \xi_{S0}/COP_{CoC} \tag{77}$$

$$\xi_{S3,A,E} + \xi_{S3,A,C}/COP_{CoC} \geq \xi_{S0}/COP_{CoC} \tag{78}$$

$$\xi_{S3,B,E} + \xi_{S3,B,C}/COP_{CoC} \geq \xi_{S0}/COP_{CoC} \tag{79}$$

To describe the effectiveness of each CCP system, the criterion performance index *PI* was newly defined as follows:

$$PI_{S1} = \frac{\xi_{S1,E}\, COP_{CoC} + \xi_{S1,C}}{\xi_{S0}} \geq 1 \tag{80}$$

$$PI_{S2} = \frac{\xi_{S2,E}\, COP_{CoC} + \xi_{S2,C}}{\xi_{S0}} \geq 1 \tag{81}$$

$$PI_{S3,A} = \frac{\xi_{S3,A,E}\, COP_{CoC} + \xi_{S3,A,C}}{\xi_{S0}} \geq 1 \tag{82}$$

$$PI_{S3,A} = \frac{\xi_{S3,B,E}\, COP_{CoC} + \xi_{S3,B,C}}{\xi_{S0}} \geq 1 \quad (83)$$

If *PI* value was larger than 1, it meant that the SOFC-GT/SE/ORC-primed CCP system was more effective in simulanously satisfying both cooling and electricity demand than that of the SOFC-primed CCP reference system under the same operating condition.

5. Results and discussions

In order to evaluate the performance of SOFC-GT-primed CCP system, SOFC-SE-primed CCP system and SOFC-ORC-primed CCP system, both its efficiency and effectiveness are evaluated in this section. The thermodynamic properties of fluid flow in each CCP system are summarized in Appendix B. The effect of key parameters are examined, including current density of SOFC stack, fuel inlet temperature of SOFC stack, compression ratio of GT, type of SE, working fluid of ORC, and system part load ratio. In this study, the current density range is chosen between 4000 A/m^2 and 8000 A/m^2. This is because current density smaller than 4000 A/m^2 results in low power density of SOFC stack, while larger than 8000 A/m^2 causes low electrical efficiency [38]. The fuel inlet temperature range is chosen between 923 K and 1123 K according to the manufacturing limitation and system stability.

5.1 SOFC-GT-primed CCP system

5.1.1 Electrical efficiency, overall efficiency and electrical efficiency boost

By considering the operating stability of SOFC stack and GT, the range of compression ratio of GT is chosen between 2 and 4. Fig. 2 presents efficiency of SOFC-GT primed CCP system against different current densities and part-load ratios under various operating conditions. Fig. 2(a) shows the electrical and overall efficiencies of the SOFC-GT-primed CCP system at different $T_{f,in}$ at compression ratio π_{GT}

of 4. As the fuel inlet and operating temperature of the SOFC stack increases, the activation and ohmic overpotentials decreases due to the enhanced ionic conductivity and exchange current density (Eqs. 4 and 7). Therefore, the cell voltage and electrical efficiency of the SOFC stack increases (Eqs. 1 and 52). Since more primary energy is converted to electricity through the SOFC stack, the electrical energy generated by GT is less at higher $T_{f,in}$. Therefore, the electrical efficiency boost of the SOFC-GT set $\Delta\eta_{S1,ele}$ is lower at higher $T_{f,in}$ accordingly.

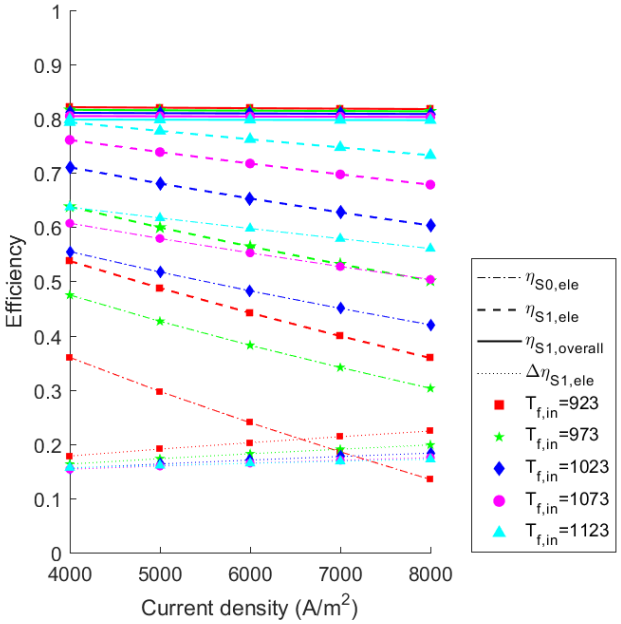

(a) Under different fuel inlet temperatures at compression ratio of 4.

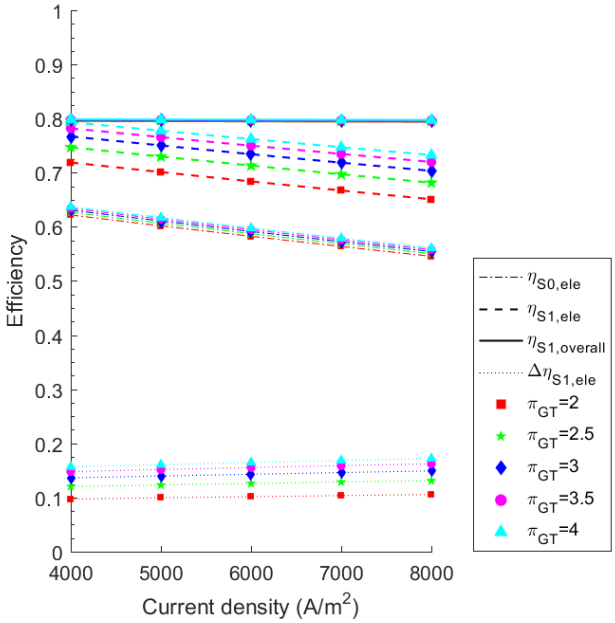

(b) Under different compression ratios at fuel inlet temperature of 1123 K.

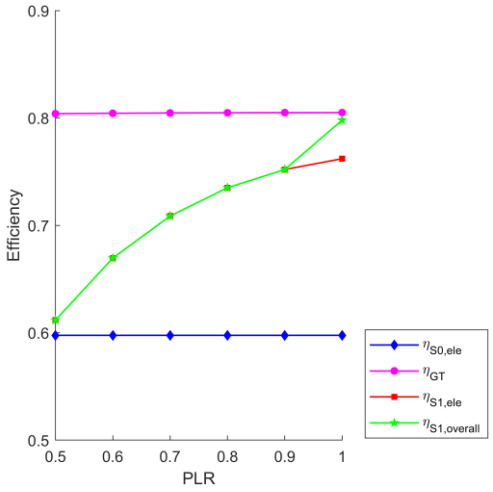

(c) Under fuel inlet temperature of 1123 K, current density of 6000 A/m^2 and compression ratio of 4.

Fig. 2. Efficiency of SOFC-GT-primed CCP system against different current densities and part-load ratios under various operating conditions.

Moreover, higher current density results in larger electrical efficiency boost due to larger mass fluid flow rate through GT. When current density is 8000 A/m^2, the largest and smallest electrical efficiency boost is 22.4% at $T_{f,in}$ = 923 K and 17.2% at $T_{f,in}$ = 1123 K, respectively. In addition, the overall efficiency is similar at different current densities and fuel inlet temperatures, since the unutilized energy in the SOFC-GT set is converted into thermal energy for cooling purpose.

Fig. 2(b) presents the electrical and overall efficiency of the SOFC-GT-primed CCP system at different compression ratios π_{GT} when fuel inlet temperature $T_{f,in}$ is kept at 1123 K. At higher operating pressure, the open circuit voltage and electrical efficiency of the SOFC stack increases. Meanwhile, larger compression ratio π_{GT} results in higher electrical power output of GT. Thus, the electrical efficiency boost of SOFC-GT set $\Delta\eta_{S1,ele}$ increases.

Fig. 2(c) illustrates the electrical and overall efficiencies of the SOFC-GT-primed CCP system at different *PLR*s when fuel inlet temperature $T_{f,in}$ is 1123 K and compression ratio π_{GT} is 4. Since the air compressor is always operated at full-load, its power consumption remains constant. As a result, total power output of the SOFC-GT set increases at higher *PLR*. When $PLR \leq 0.4$, $P_{GT} \leq P_{com}$, which results in low or even negative electrical efficiency. Thus, *PLR* is set larger or equal to 0.5. The electrical efficiency of the SOFC stack and GT is almost constant at different *PLR*s. When *PLR* is smaller than 0.9, the temperature of exhaust gas would be lower than 373 K, which is not sufficient to satisfy the thermal energy of AbC. Therefore, the overall efficiency equals to the electrical efficiency when $PLR \leq 0.9$. When $PLR = 1$, the temperature of exhaust gas is 634 K as shown in Table B.1 (in Appendix B), which can be used to supply thermal energy for AbC. Since the overall efficiency is higher than the electrical efficiency, there exists an abrupt change in overall efficiency when changing *PLR* from 0.9 to 1.

5.1.2 *PI* values

Fig. 3 depicts *PI* values of SOFC-GT-primed CCP system against different current densities and part-load ratios under various operating conditions. Figs. 3(a) and (b) show the effects of fuel inlet temperature, compression ratio and current density on the *PI* value of the SOFC-GT-primed CCP system. From Figs. 2(a) and (b), lower current density, higher fuel inlet temperature and higher compression ratio results in higher electrical efficiency of the SOFC stack and SOFC-GT set. Since

the GT directly expands the pressurized exhaust gas to boost electricity production, *PI* value increases with the decrease of current density, increase of fuel inlet temperature and increase of compression ratio accordingly. The highest *PI* value achieves 3.2 when current density is 4000 A/m^2, fuel inlet temperature is 1123 K and compression ratio is 4.

Figs. 3(c)-(f) show the effects of fuel inlet temperature, compression ratio, current density and COP_{CoC} on the *PI* value of the SOFC-GT-primed CCP system when it is operated at various part-load conditions. *PI* value of the SOFC-GT-primed CCP system decreases with the decrease of *PLR* due to lower electrical efficiency. At different *PLR*s, the *PI* value also increases with the increase of fuel inlet temeperature, the increase of compression ratio, the decrease of current density and the increase of COP_{CoC}. When *PLR* is less than 0.6, *PI* value is less than 1 under most of the operating conditions. This means that the SOFC-GT-primed CCP system is not as effective as the SOFC-primed CCP reference system.

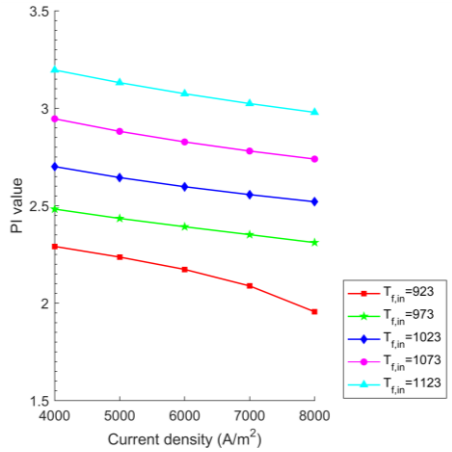

(a) Under different fuel inlet temperatures at compression ratio of 4.

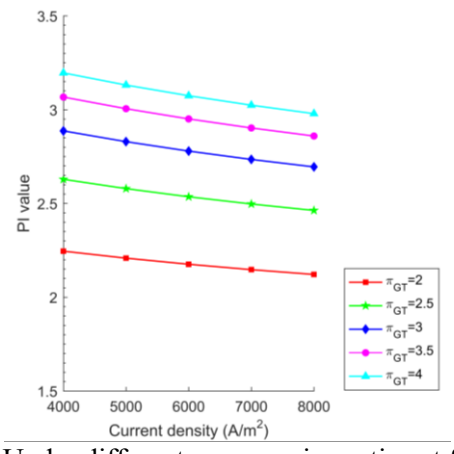

(b) Under different compression ratios at fuel inlet temperature of 1123 K.

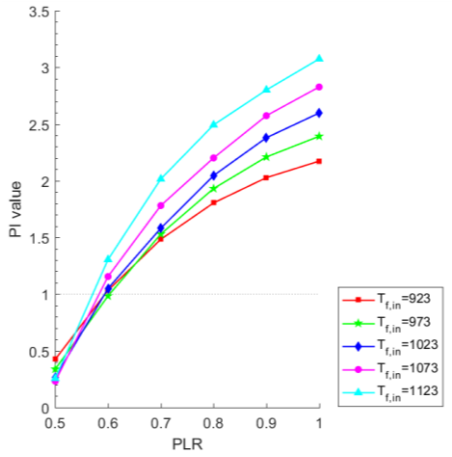

(c) Under different fuel inlet temperatures at current density of 6000 A/m^2, compression ratio of 4, and COP_{CoC} of 5.

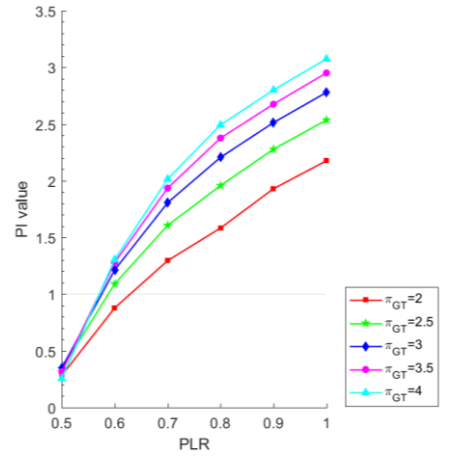

(d) Under different compression ratios at current density of 6000 A/m^2, fuel inlet temperature of 1123 K, and COP_{CoC} of 5.

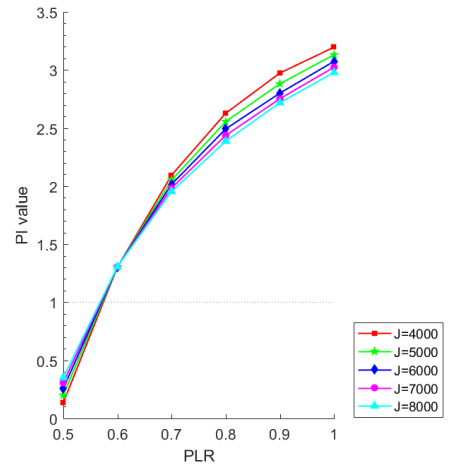

(e) Under different current densities at fuel inlet temperature of 1123 K, compression ratio of 4 and COP_{CoC} of 5.

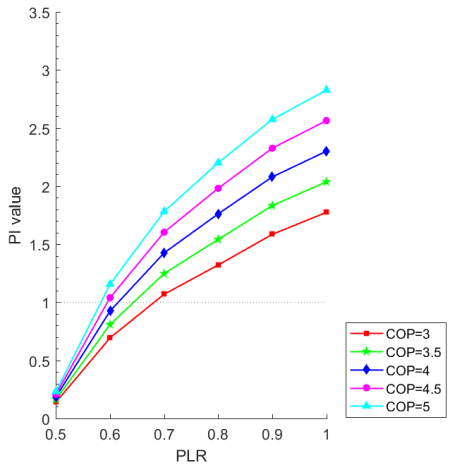

(f) Under different COP_{CoC} at fuel inlet temperature of 1123 K, current density of 6000 A/m^2, and compression ratio of 4.

Fig. 3. *PI* values of SOFC-GT-primed CCP system against different current densities and part-load ratios under various operating conditions.

5.2 SOFC-SE-primed CCP system

5.2.1 Electrical efficiency, overall efficiency and electrical efficiency boost

Fig. 4 illustrates efficiency of SOFC-SE-primed CCP system against different current densities and part-load ratios under various operating conditions. Fig. 4(a) shows the electrical and overall efficiencies of the SOFC-SE-primed CCP system at different fuel inlet temperatures when using α-SE. In the SOFC-SE-primed CCP system, the SOFC stack operates at ambinet preussure. Therefore, at identical current density and operating temperature, the electrical efficiency of the SOFC stack is slightly smaller than that in the SOFC-GT-primed CCP system. When fuel inlet temperature is lower than 1023 K, the electrical efficiency boost of SOFC-SE-primed CCP system is slightly higher (in the range of [0.2, 0.4]) compared to that of SOFC-GT-primed CCP system (in the range of [0.15, 0.25]) due to better thermal energy utization ability through the SE. When fuel inlet temperature is higher than 1023 K, the electrical efficiency boost of the SOFC-SE-primed CCP system becomes lower than that of the SOFC-GT-primed CCP system. The overall efficiency of the SOFC-SE-primed CCP system is relatively constant under different operating conditions since both the exhaust gas after the pre-heaters and from the cold side of the SE is utilized to provide thermal energy for the AbC.

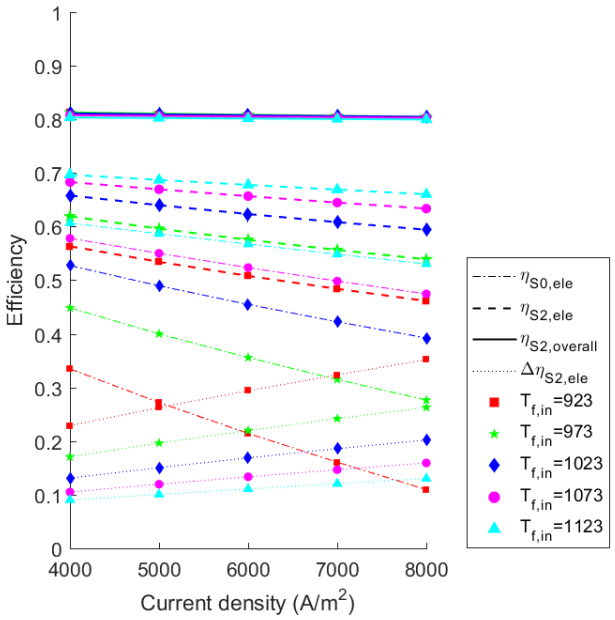

(a) Under different fuel inlet temperatures for α-SE.

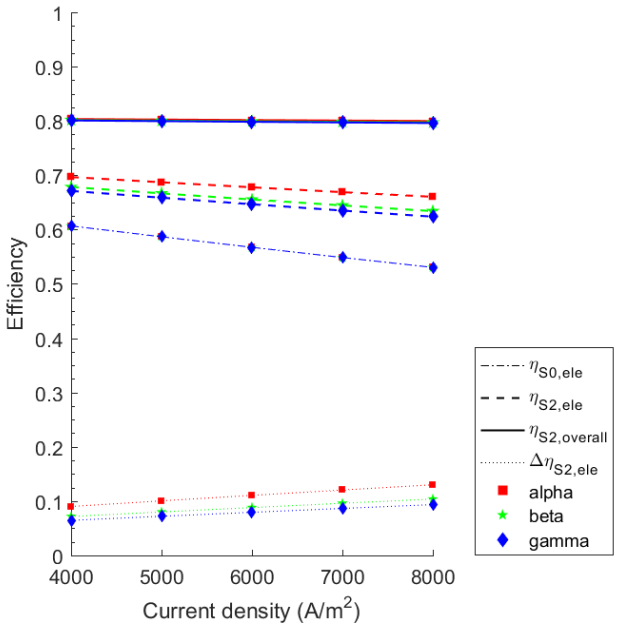

(b) Under fuel inlet temperature of 1123 K for different types of SE at.

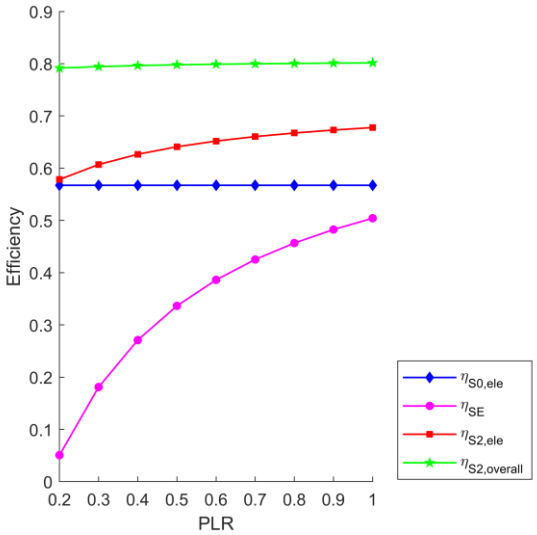

(c) Under fuel inlet temperature of 1123 K and current density of 6000 A/m^2 for α-SE.

Fig. 4. Efficiency of SOFC-SE-primed CCP system against different current densities and part-load ratios under various operating conditions.

Fig. 4(b) presents the electrical and overall efficiencies of the SOFC-SE-primed CCP system using α-SE, β-SE and γ-SE, respectively. Since the electrical efficiency of α-SE is the highest while γ-SE is the lowest, the expected trend is identical for the electrical efficiency boost of the SOFC-SE-primed CCP system using these three types of SE.

Fig. 4(c) illustrates the electrical and overall efficiencies of the SOFC-SE-primed CCP system at different *PLR*s when $T_{f,in}$ = 1123 K and using α-SE. At lower *PLR*, the recoverable heat from the burner decreases due to smaller operating quantity of SOFC stacks. If *PLR* is smaller than 0.2, the recovered thermal energy is not sufficient to drive the SE. Since the elctrical efficiency of SE is affected by the temperature of the hot source, the electrical effiency of the SE and the SOFC-SE set decreases at lower *PLR*.

5.2.2 *PI* values

Fig. 5 consolidates *PI* values of SOFC-SE-primed CCP system against different current densities and part-load ratios under various operating conditions. Figs. 5(a) and (b) show the effects of fuel inlet temperature, type of SE and current density on the *PI* value of the SOFC-SE-primed CCP system. At lower fuel inlet temperature and higher current density, the electrical efficiency of the SOFC stack is lower. Therefore, more thermal energy from the burner and the cold side of SE can be recovered for the SE. Thus, *PI* value increases with the decrease of fuel inlet temeperature. Meanwhile, higher electrical efficiency of α-SE results in higher *PI* value of the SOFC-SE-primed CCP system. The highest *PI* value achieves 3.2 when current density is 8000 A/m^2, fuel inlet temperature is 923 K and α-SE is used.

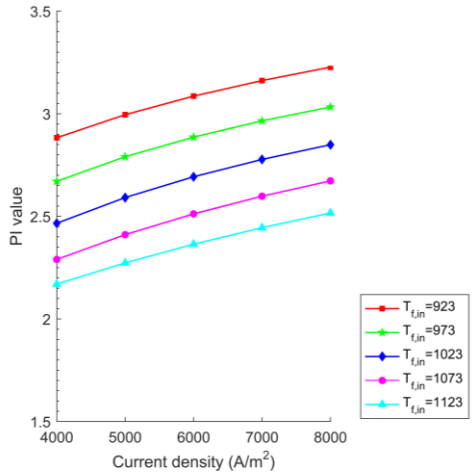

(a) Under different fuel inlet temperatures for α-SE.

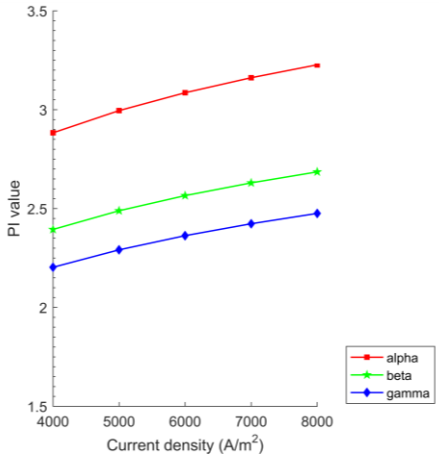

(b) Under fuel inlet temperature of 923 K for different types of SE.

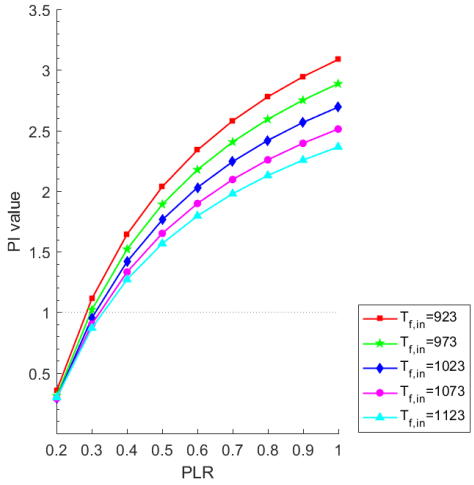

(c) Under different fuel inlet temperatures at current density of 6000 A/m^2 and COP_{CoC} of 5 for α-SE.

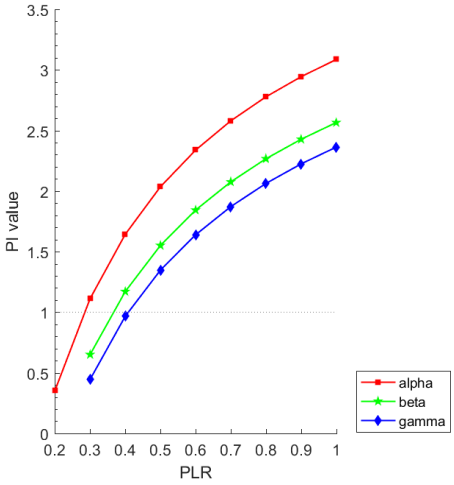

(d) Under fuel inlet temperature of 923 K, current density of 6000 A/m^2 and COP_{CoC} of 5 for different types of SE.

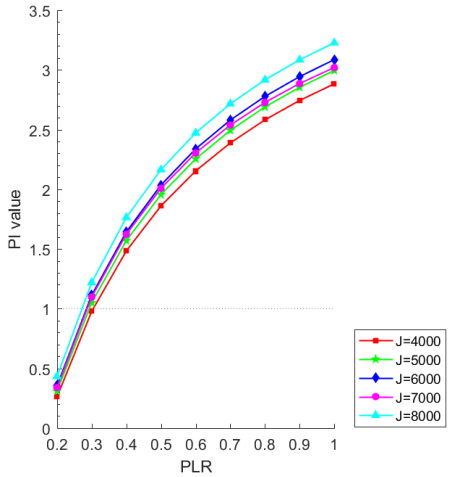

(e) Under different current densities at fuel inlet temperature of 923 K and COP_{CoC} of 5 for α-SE.

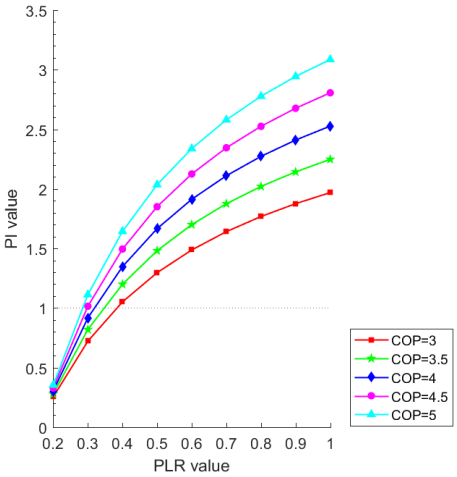

(f) Under different COP_{CoC} at fuel inlet temperature of 923 K and current density of 6000 A/m^2 for α-SE.

Fig. 5. *PI* values of SOFC-SE-primed CCP system against different current densities and part-load ratios under various operating conditions.

Figs. 5(c)-(f) show the effects of fuel inlet temperature of SOFC stack, configuration type of SE, current density of SOFC stack and COP_{CoC} on the *PI* value of the SOFC-SE-primed CCP system when it is operated at part-load. *PI* value of SOFC-SE CCP system decreases with the decrease of *PLR* owing to its lower electrical efficiency. For SOFC-SE-primed CCP system using α-SE, when $PLR \leq 0.4$, *PI* value declines to smaller than 1 due to the low electrical efficiency of SE. For SOFC-SE-primed CCP systems using β-SE or γ-SE, *PI* value is smaller than 1 when $PLR \leq 0.5$.

5.3 SOFC-ORC-primed CCP system

5.3.1 Electrical efficiency, overall efficiency and electrical efficiency boost

Fig. 6 depicts efficiency of SOFC-ORC-primed CCP system against different current densities and part-load ratios under various operating conditions. Fig. 6(a) shows the electrical and overall efficiencies of the SOFC-ORC-primed CCP system at different fuel inlet temperatures when o-Xylene was used as the working fluid. Due to lower electrical efficiency of ORC compared to SE, the eletrical efficiency boost of SOFC-ORC-primed CCP system is lower (in the range [0, 0.1]). For A-type SOFC-ORC-primed CCP system, the heat rejected by the ORC condenser is further used to drive the AbC, thus results in higher and relatively constant overall efficiency. For B-type SOFC-ORC-primed CCP system, since the temperature difference between the evaporator and condenser is higher than that of A-type under the same operating condition, the electrical efficinecy of the ORC thus the electrical efficiency boost of SOFC-ORC set is approximately 2% higher.

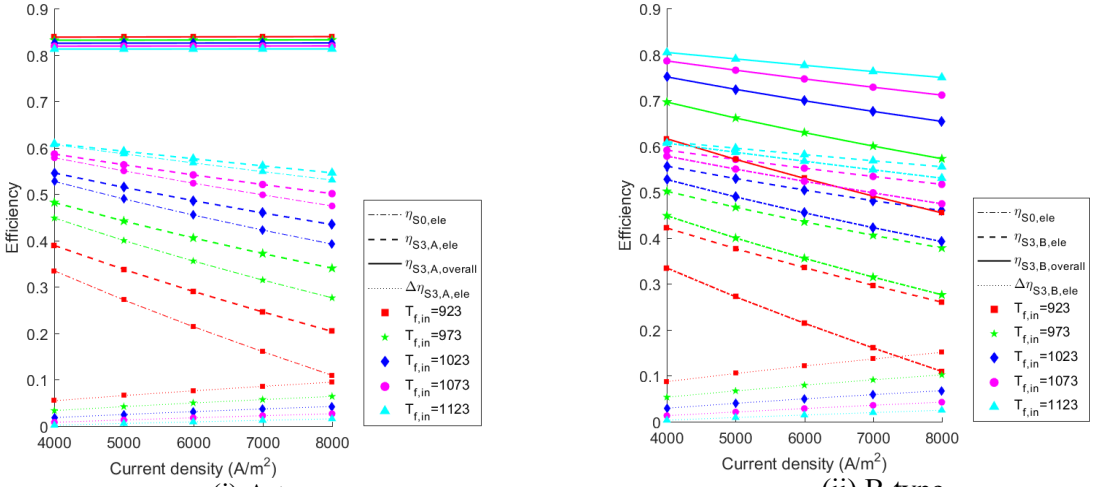

(i) A-type (ii) B-type

(a) Under different fuel inlet temperatures for using o-Xylene as working fluid.

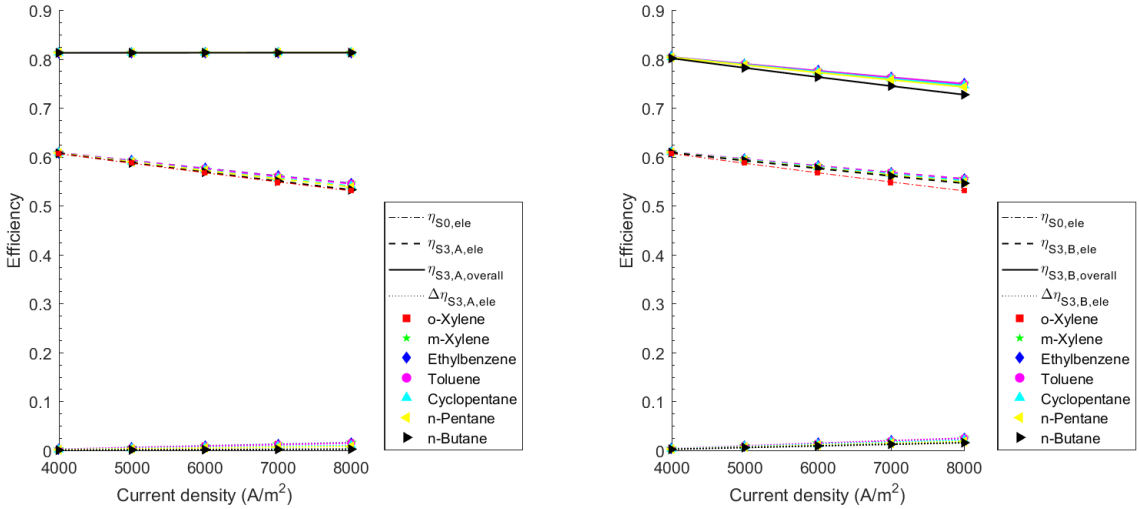

(i) A-type (ii) B-type

(b) Under fuel inlet temperature of 1123 K for using different working fluids.

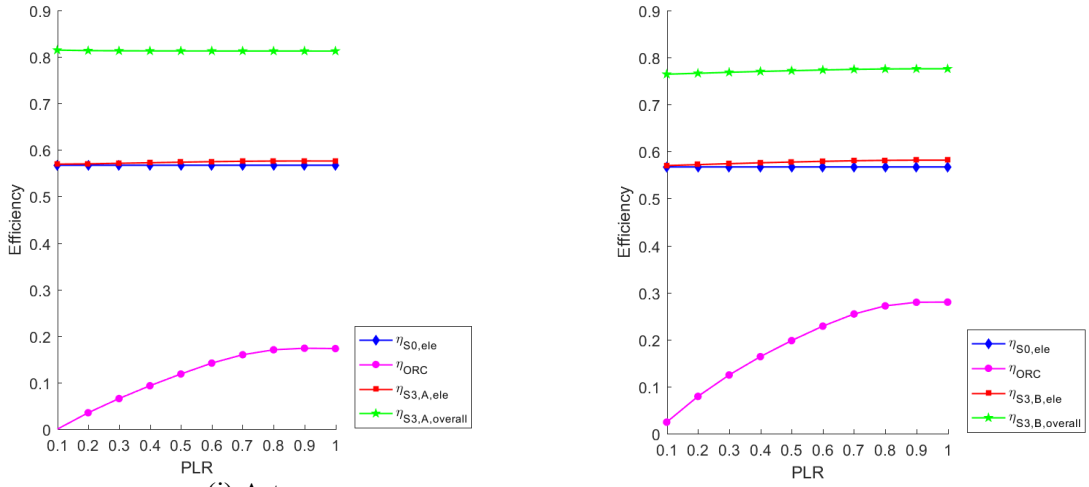

(i) A-type (ii) B-type

(c) Under fuel inlet temperature of 1123 K and current density of 6000 A/m^2 for using o-Xylene.

Fig. 6. Efficiency of SOFC-ORC-primed CCP system against different current densities and part-load ratios under various operating conditions.

Fig. 6(b) presents the electrical and overall efficiencies of the SOFC-ORC-primed CCP system when using different working fluids in ORC. Although the critical temperature of the working fluids is different [43], the electrical efficiency of the ORC is similar. Moreover, the electrical efficiency boost is in the range of [0, 0.03], distinctly lower than those in SOFC-GT- and SOFC-SE-primed CCP systems.

Fig. 6(c) illustrates the electrical and overall efficiencies of the SOFC-ORC-primed CCP system at different *PLR*s when $T_{f,in}$ = 1123 K and using o-Xylene. At lower *PLR*, the recoverable heat from the burner, thus the ORC evaporator temperature and its electrical efficiency decreases. The overall efficiency is relatively constant at different *PLRs* due to the utilization of thermal energy from the exhaust gas.

5.3.2 *PI* values

Fig. 7 shows the effects of fuel inlet temperature of SOFC stack and working fluid of ORC on the *PI* value of the SOFC-ORC-primed CCP system respectively. As shown in Fig. 7(a), the *PI* value of B-type SOFC-ORC-primed CCP system is higher than that of the A-type, especially at lower inlet fuel temperature. It is because more primary energy of the fuel is converted into electrical energy. When fuel inlet temperature is higher than 1023 K, *PI* value of the SOFC-ORC-primed CCP system is lower than 1, which means that it is not as effective as the SOFC-primed CCP reference system. From Fig. 7(b), for A-type SOFC-ORC-primed CCP system, *PI* value of n-Butane and n-Pentane is always smaller than 1. For B-type SOFC-ORC-primed CCP system, *PI* value is smaller than 1 only when n-Butane is used as the working fluid and when current density is lower than 7000 A/m^2. It is because that the critical temperature of n-Butane is the lowest [43].

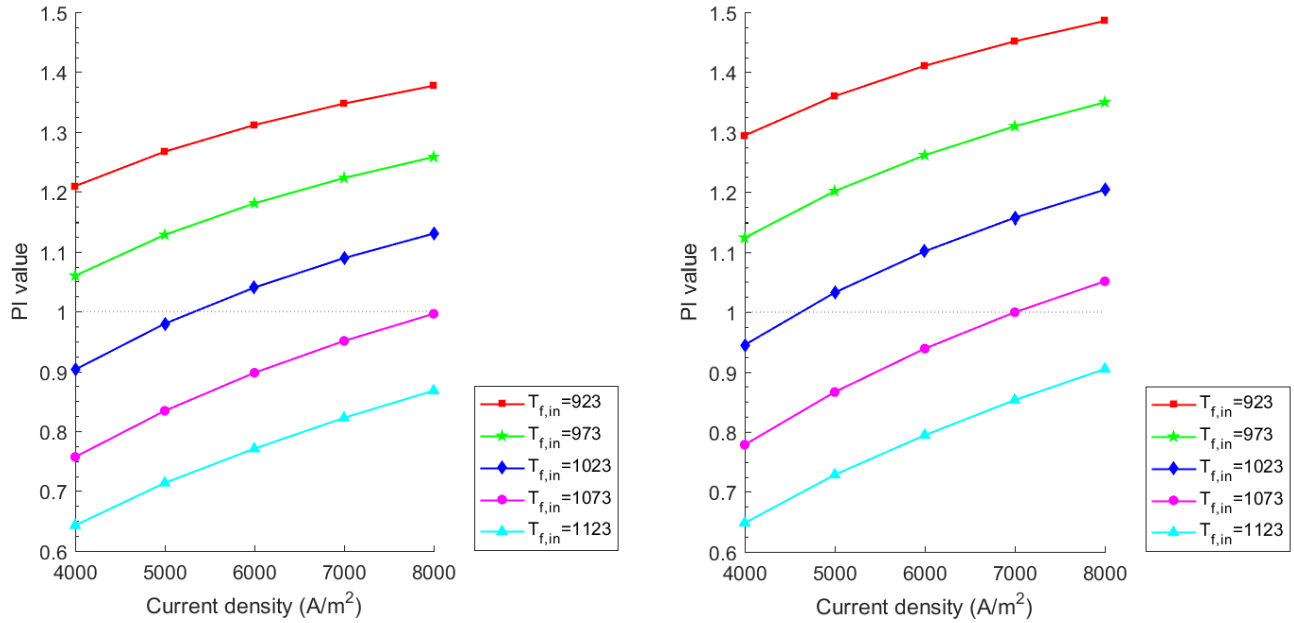

(i) A-type (ii) B-type

(a) Under different fuel inlet temperatures for using o-Xylene as working fluid.

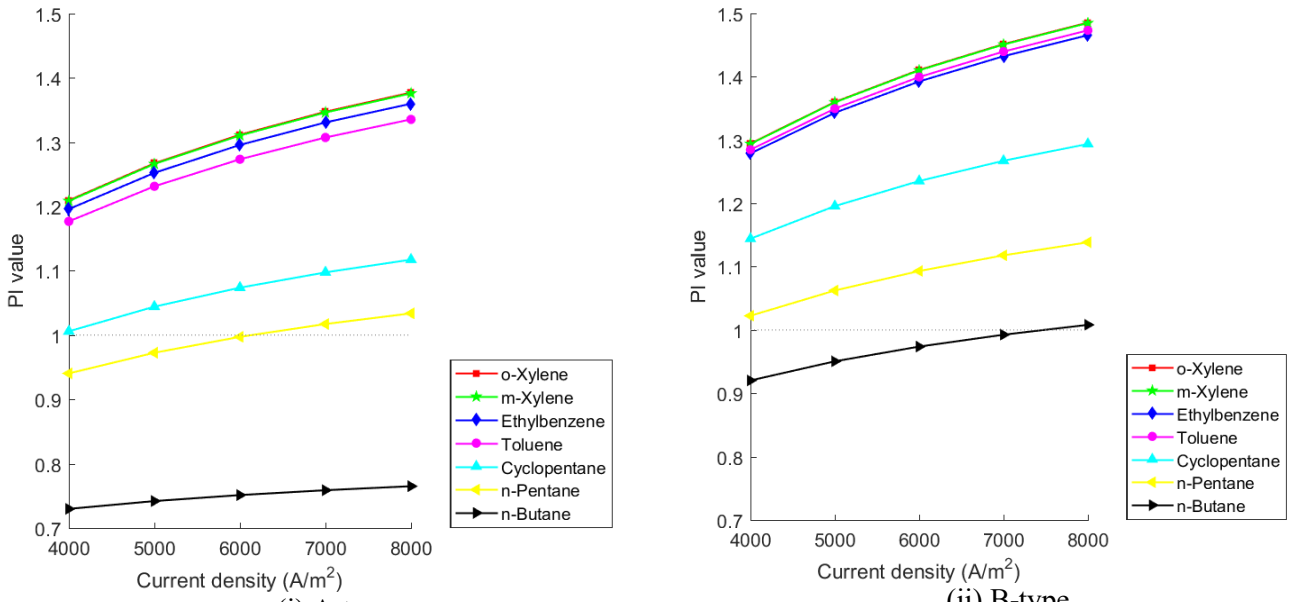

(i) A-type (ii) B-type

(b) Under fuel inlet temperature of 923 K for using different working fluids.

Fig. 7. *PI* values of SOFC-ORC-primed CCP system against different current densities under various operating conditions.

Fig. 8 shows the effects of fuel inlet temperature of SOFC stack, working fluid of ORC, current density of SOFC stack and COP_{CoC} on the *PI* value of SOFC-ORC-primed CCP system when it is at part-load operation. When *PLR* is lower than 0.6, *PI* value of A-type SOFC-ORC-primed CCP system is higher than that of B-type, and vice versa. It is because that the electrical efficiency of ORC

decreases during part-load operation. n-Butane has the lowest critical temperature, thus results in the lowest electrical efficiency and *PI* value of SOFC-ORC-primed CCP system. For both A-type and B-type SOFC-ORC-primed CCP systems, *PI* value reaches peak when *PLR* = 0.9 when fuel inlet temperature is 923 K, and decreases a little after that. This is mainly due to the characteristics of ORC turbine. In most of the cases, *PI* value decreases to lower than 1 when $PLR \leq 0.3$.

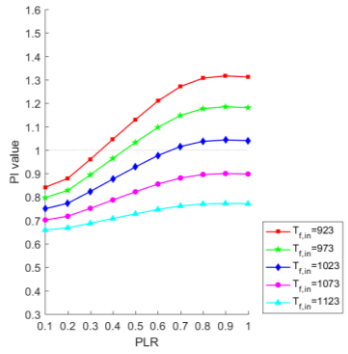

(i) A-type

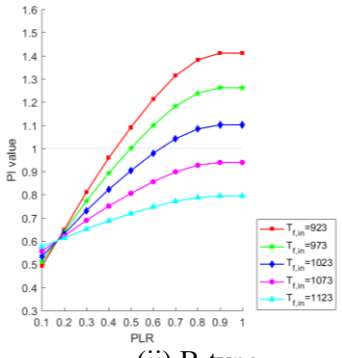

(ii) B-type

(a) Under different fuel inlet temp. at current density of 6000 A/m^2 and COP_{CoC} of 5 for o-Xylene.

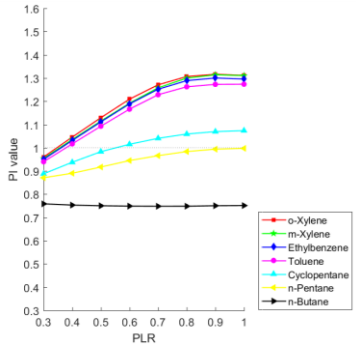

(i) A-type

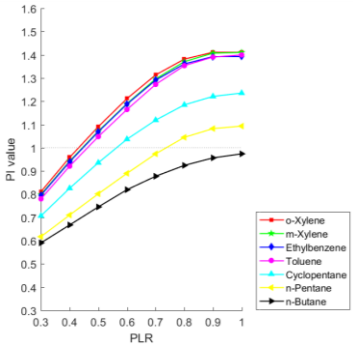

(ii) B-type

(b) Under fuel inlet temperature of 923 K, current density of 6000 A/m^2 and COP_{CoC} of 5.

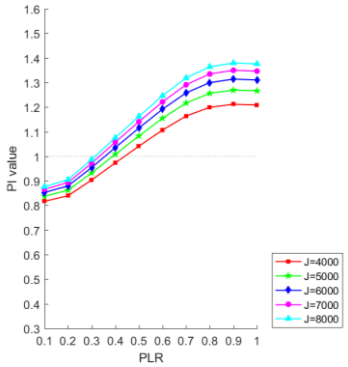

(i) A-type

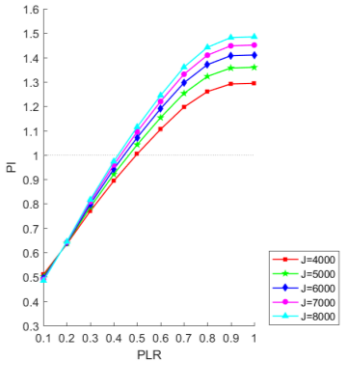

(ii) B-type

(c) Under different current densities at fuel inlet temperature of 923 K and COP_{CoC} of 5 for o-Xylene.

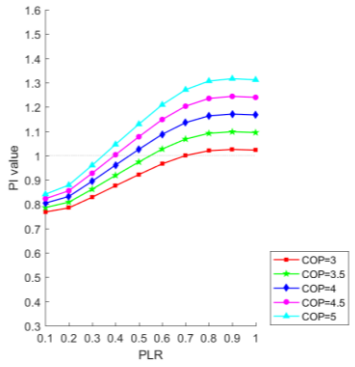

(i) A-type

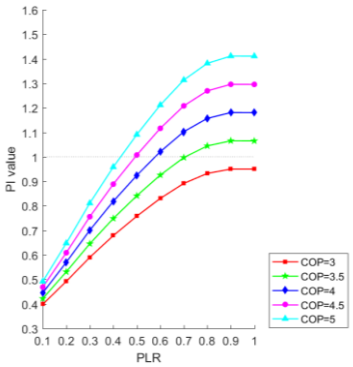

(ii) B-type

(d) Under different COP_{CoC} , fuel inlet temp. of 923 K and current density of 6000 A/m^2 for o-Xylene.

Fig. 8. *PI* values of SOFC-ORC-primed CCP system against different part-load ratios under various operating conditions.

6. Conclusion

In order to satisfy high cooling and electricity demands in buildings in hot-humid areas, conventional trigeneration system was refined to CCP system. For electricity production, SOFC stack was connected with different bottoming cycles to serve as the prime mover set. For cooing production, AbC was adopted to utilize the recovered thermal energy while CoC was driven by the electrical energy generated from the prime mover set. To systematically evaluate the CCP system performance under different operating and loading conditions, thermodynamic models of key equipment units including SOFC stack, GT, SE and ORC were developed with consideration of part-load operation. The effects of fuel inlet temperature and current density of SOFC stack; compression ratio of GT; types of SE; working fluids in ORC; and SOFC stack part-load ratio on both effciencies and effectiveness of the corresponding CCP systems were fully assessed. The key findings are highlighted as follows:

- For the SOFC-GT-primed CCP system, higher fuel inlet temperature and smaller current density results in both higher electrical efficiency and higher system effectiveness. Therefore, high fuel inlet temperature and small current density should be chosen at the design stage. But the material stability of both SOFC stack and GT should be considered when increasing its operating temperature.
- For the SOFC-SE-primed CCP system, lower fuel inlet temperature results in higher electrical efficiency and higher system effectiveness. Meanwhile, lower current density results in higher electrical efficiency but lower effectiveness when simultaneously supplying cooling and electricity. Therefore, when cooling plays a significant role in building energy demand, it is recommended that the SOFC-SE-primed CCP system should be designed at low fuel inlet temperature and small current density.
- For the SOFC-ORC-primed CCP system, higher fuel inlet temperature and lower current density results in higher electrical efficiency but lower system efficiency. When the ratio between

cooling and electricity demand is high, it is recommened that the SOFC-ORC-primed CCP system should be operated at low fuel inlet temperature and high current density.

- For the SOFC-ORC-primed CCP systems, although the overall efficiency can be improved through recovering the thermal energy in ORC for cooling purpose, its electrical efficiency and system effectiveness would be lower. Thus, it is recommended that low condenser temperature of ORC (i.e. B-type SOFC-ORC-primed CCP system) should be chosen to fully utilize its feature in electricity generation.
- For the SOFC-GT-primed CCP system, larger compression ratio of GT results in higher electrical efficiency and system effectiveness. For the SOFC-SE-primed CCP system, the SOFC-SE set using α-SE has the largest electrical efficiency and system effectiveness. For the SOFC-ORC-primed CCP system, although the electrical efficiency is relatively independent on the types of working fluids, o-Xylene and m-Xylene would have the largest system effectiveness. Thus, it is suggested that high compression ratio of GT should be chosen for the SOFC-GT-primed CCP system; α-SE should be adopted for the SOFC-SE-primed CCP system; and o-Xylene or m-Xylene should be used as working fluid for the SOFC-ORC-primed CCP system.
- When inlet fuel temperature is lower than 1023 K, the SOFC-SE-primed set has higher electrical efficiency boost than that of the SOFC-GT-primed set, and vice versa. The SOFC-ORC-primed set always has the smallest electrical efficiency boost owing to the low electrical efficiency of ORC.
- At full-load operation, the highest possible electrical efficiency is 80% and 70% for the SOFC-GT-primed CCP system and the SOFC-SE-primed CCP system, respectively; while the *PI* value is around 3.2 for both the SOFC-GT and SOFC-SE-primed CCP systems. For the SOFC-GT-primed CCP system at current density of 6000 A/m^2, the electrical efficiency is decreased from 76% to 61% while *PI* value decreased from and 3.1 to 0.2 when *PLR* is reduced from 1 to 0.5. For the SOFC-SE-primed CCP system at current density of 6000 A/m^2, the electrical efficiency is decreased from 68% to 58% while *PI* value decreaed from 3.1 to 2.1 when *PLR* is reduced from 1 to 0.2. Therefore, when the cooling and electricity demands are relatively constant, the

SOFC-GT-primed CCP system is a good option due to its high electrical efficiency and system effectiveness. However, when variation of energy demands is large due to changing outdoor weather conditions, the SOFC-SE-primed CCP system serves as a good choice.

- *PI* value of different CCP systems may decrease to less than 1 at low *PLR* under different current densities, fuel inlet temperatures and COP_{CoC}. It is found that *PI* value is less than 1 when *PLR* is 0.6, 0.4 and 0.3 for the SOFC-GT-primed CCP system, the SOFC-SE-primed CCP system and the SOFC-ORC-primed system, respectively. It is suggested that the bottoming cycle should be bypassed in order not to defeat the effectiveness of the corresponding CCP system in such circumstance.
- SOFC-ORC-primed CCP system would be a suitable choice for medium-temperature SOFC stack, since the temperature of exhaust heat required by the ORC evaporator is around 600 K, which is much lower than those in SOFC-GT and SOFC-SE sets.

Acknowledgement

This work described in this paper is fully supported by a grant from the Research Grants Council of the Hong Kong Special Administrative Region, China (Project No. CityU 11200315).

Nomenclature

List of abbreviations

AbC	Absorption chiller
CCHP	Combined cooling, heating and power
CCP	Combined cooling and power
CHP	Combined heat and power
CoC	Compression chiller
COP	Coefficient of performance
GT	Gas turbine

MSR	Methane steam reforming
ORC	Organic Rankine cycle
SE	Stirling engine
SOFC	Solid oxide fuel cell
WGS	Water gas shifting

List of symbols

A	Surface area of SOFC stack (m^2)
B_I, B_{II}, B_{III}	Coefficients of GT
C_p	Specific heat ($J \cdot kg^{-1}K^{-1}$)
COP	Coefficient of performance
d	Thickness (m)
D	Energy demand ($GJ \cdot h^{-1}$)
F	Faraday constant ($96485A \cdot s \cdot mol^{-1}$)
h	Specific enthalpy ($J \cdot mol^{-1}$ in SOFC stack model, $kJ \cdot kg^{-1}$ in GT model)
J	Current density ($A \cdot m^{-2}$)
k	Thermal conductivity ($W \cdot K^{-1}m^{-1}$)
LHV	Lower heating value ($J \cdot mol^{-1}$)
m	Mass flow rate ($kg \cdot h^{-1}$)
n	Molar flow rate ($mol \cdot s^{-1}$)
N	Quantity of SOFC sub-stacks
p	Pressure (Pa)
P	Electrical power ($kJ \cdot kg^{-1}$)
PI	Performance index
PLR	Part-load ratio
q	Molar heat rate ($kJ \cdot h^{-1}$)
Q	Heat transfer rate ($kJ \cdot h^{-1}$)
r	Reaction rate for chemical/electrochemical reactions ($mol \cdot m^{-3}s^{-1}$)

R	Gas constant (8.314 $m^3 \cdot Pa \cdot K^{-1} mol^{-1}$)
s	Specific entropy ($J \cdot mol^{-1}\ K^{-1}$)
S	Source terms in SOFC model
T	Temperature (K)
U	Voltage (V)
u	Velocity of fluid flow along x direction of SOFC ($m \cdot s^{-1}$)
V	Volume (m^3)
v	Velocity of fluid flow along z direction of SOFC ($m \cdot s^{-1}$)
Y	Mass fraction
σ	Effective diffusion coefficient of each gas species ($m^2 \cdot s^{-1}$)
ρ	Density of the gas mixture ($kg \cdot m^{-3}$)
η	Efficiency (%)
ξ	Contribution ratio
π	Compression ratio
ε	Effectiveness
$\Delta\eta$	Electrical efficiency boost

List of subscripts

1, 2, …, 23	State points in Fig. 1
a	Air
A	A-type ORC
ac	Air channel
act	Activation
an	Anode
an-ely	Interface between anode and electrolyte
AbC	Absorption chiller
B	B-type ORC
bu	Burner

c	Compression in the SE
C	Cooling energy
ca	Cathode
ca-ely	Interface between cathode and electrolyte
CoC	Compression chiller
com	Air compressor
cycle	Thermodynamic cycle in SE
d	Dead volume in SE
e	Expansion in the SE
E	Electrical energy
ele	Electrical efficiency
ely	Electrolyte
ex	Exchange current density
exh	Exhaust
f	Fuel
fc	Fuel channel
fl	Full-load operation
GT	Gas turbine
H	Hot source in the SE
he	Heater in the SE
hf	Hot fluid
in	Inlet
is	Isentropic
L	Cold source
m	Methane
mech	Mechanical
mi	Gas species
mt	Total mass source rate

MSR	Methane steam reforming
oc	Open circuit
ohm	Ohmic
out	Outlet
*p*0	Ambient pressure
PH	Pre-heater
pl	Part-load operation
re	Reformer
reg	Regenerator in the SE
s	Swept volume in the SE
*S*0	SOFC-primed CCP reference system
*S*1	SOFC-GT-primed CCP system
*S*2	SOFC-SE-primed CCP system
*S*3	SOFC-ORC-primed CCP system
tur	ORC turbine
w	Water
wf	Working fluid
WGS	Water gas shifting

References

[1] E. Achenbach, Report IEA Programme on Advanced Fuel Cells Annex II, International Energy Agency, Juelich, 1996.

[2] Braun R, Kazempoor P. Application of SOFCs in combined heat, cooling, and power systems. Solid Oxide Fuel Cells: From Materials to System Modeling. Energy and Environment Series, (2013)327-382.

[3] Calise F, d'Accadia MD, Palombo A, Vanoli L. Simulation and exergy analysis of a hybrid solid oxide fuel cell (SOFC)–gas turbine system. Energy, 31(2006)3278-99.

[4] Zhao Y, Sadhukhan J, Lanzini A, Brandon N, Shah N. Optimal integration strategies for a syngas fuelled SOFC and gas turbine hybrid. Journal of Power Sources, 196(2011)9516-27.

[5] Selimovic A, Palsson J. Networked solid oxide fuel cell stacks combined with a gas turbine cycle. Journal of Power Sources, 106(2002)76-82.

[6] Chinda P, Brault P. The hybrid solid oxide fuel cell (SOFC) and gas turbine (GT) systems steady state modeling. International Journal of Hydrogen Energy, 37(2012)9237-48.

[7] Cheng T, Jiang J, Wu X, Li X, Xu M, Deng Z and Li J. Application oriented multiple-objective optimization, analysis and comparison of solid oxide fuel cell systems with different configurations. Applied energy, 235(2019)914-929.

[8] Jia J, Shu L, Zang G, Xu L, Abudula A and Ge K. 2018. Energy analysis and techno-economic assessment of a co-gasification of woody biomass and animal manure, solid oxide fuel cells and micro gas turbine hybrid system. Energy, 149(2018)750-761.

[9] Chan SH, Ho HK, Tian Y. Multi-level modeling of SOFC–gas turbine hybrid system. International Journal of Hydrogen Energy, 28(2003)889-900.

[10] Barelli L, Bidini G, Ottaviano A. Part load operation of SOFC/GT hybrid systems: stationary analysis. International Journal of Hydrogen Energy, 37(2012)16140-50.

[11] Chan SH, Ho HK, Tian Y. Modelling for part-load operation of solid oxide fuel cell–gas turbine hybrid power plant. Journal of Power Sources, 114(2003)213-27.

[12] Martinez AS, Brouwer J, Samuelsen GS. Feasibility study for SOFC-GT hybrid locomotive power: Part I. Development of a dynamic 3.5 MW SOFC-GT FORTRAN model. Journal of Power Sources, 213(2012)203-17.

[13] Calise F, d'Accadia MD, Vanoli L, Von Spakovsky MR. Single-level optimization of a hybrid SOFC–GT power plant. Journal of Power Sources, 159(2006)1169-85.

[14] Costamagna P, Magistri L, Massardo AF. Design and part-load performance of a hybrid system based on a solid oxide fuel cell reactor and a micro gas turbine. Journal of Power Sources, 96(2001)352-68.

[15] Tse LKC, Wilkins S, McGlashan N, Urban B and Martinez-Botas R. Solid oxide fuel cell/gas turbine trigeneration system for marine applications. Journal of Power Sources, 196(2011)3149-3162.

[16] Mahmoudi SMS and Khani L. Thermodynamic and exergoeconomic assessments of a new solid oxide fuel cell-gas turbine cogeneration system. Energy Conversion and Management, 123(2016)324-337.

[17] Sanaye S and Katebi A. 4E analysis and multi objective optimization of a micro gas turbine and solid oxide fuel cell hybrid combined heat and power system. Journal of Power Sources, 247(2014)294-306.

[18] Khani L, Mehr AS, Yari M and Mahmoudi SMS. Multi-objective optimization of an indirectly integrated solid oxide fuel cell-gas turbine cogeneration system. International Journal of Hydrogen Energy, 41(2016)21470-21488.

[19] Burer M, Tanaka K, Favrat D and Yamada K. Multi-criteria optimization of a district cogeneration plant integrating a solid oxide fuel cell–gas turbine combined cycle, heat pumps and chillers. Energy, 28(2003)497-518.

[20] Chen L, Gao S and Zhang H. Performance analysis and multi-objective optimization of an irreversible solid oxide fuel cell-stirling heat engine hybrid system. International Journal of Electrochem Science, 8(2013)10772-10787.

[21] Hosseinpour J, Sadeghi M, Chitsaz A, Ranjbar F and Rosen M.A. Exergy assessment and optimization of a cogeneration system based on a solid oxide fuel cell integrated with a Stirling engine. Energy Conversion and Management, 143(2017)448-458.

[22] Xu H, Chen B, Tan P, Zhang H, Yuan J, Liu J and Ni M. Performance improvement of a direct carbon solid oxide fuel cell system by combining with a Stirling cycle. Energy, 140(2017)979-987.

[23] Rokni M. Biomass gasification integrated with a solid oxide fuel cell and Stirling engine. Energy, 77(2014)6-18.

[24] Rokni M. Thermodynamic and thermoeconomic analysis of a system with biomass gasification, solid oxide fuel cell (SOFC) and Stirling engine. Energy, 76(2014)19-31.

[25] Rokni M. Plant characteristics of a multi-fuel SOFC-Stirling hybrid configuration. SEEP, (2012)269-74.

[26] Rokni M. Thermodynamic analysis of SOFC (solid oxide fuel cell)–Stirling hybrid plants using alternative fuels. Energy, 61(2013)87-97.

[27] Habibollahzade A, Gholamian E, Houshfar E and Behzadi A. Multi-objective optimization of biomass-based solid oxide fuel cell integrated with Stirling engine and electrolyzer. Energy Conversion and Management, 171(2018)1116-1133.

[28] Kalina J. Options for using solid oxide fuel cell technology in complex integrated biomass gasification cogeneration plants. Biomass and Bioenergy, 122(2019)400-413.

[29] Ebrahimi M and Moradpoor I. Combined solid oxide fuel cell, micro-gas turbine and organic Rankine cycle for power generation (SOFC–MGT–ORC). Energy Conversion and Management, 116(2016)120-133.

[30] Akkaya AV and Sahin B. A study on performance of solid oxide fuel cell-organic Rankine cycle combined system. International Journal of Energy Research, 33(2009)553-64.

[31] Pierobon L, Rokni M, Larsen U and Haglind F. Thermodynamic analysis of an integrated gasification solid oxide fuel cell plant combined with an organic Rankine cycle. Renewable energy, 60(2013)226-234.

[32] Al-Sulaiman FA, Dincer I, Hamdullahpur F. Energy analysis of a trigeneration plant based on solid oxide fuel cell and organic Rankine cycle. International Journal of Hydrogen Energy, 35(2010)5104-13.

[33] Al-Sulaiman FA, Dincer I, Hamdullahpur F. Exergy analysis of an integrated solid oxide fuel cell and organic Rankine cycle for cooling, heating and power production. Journal of Power Sources, 195(2010)2346-54.

[34] Amicabile S, Testi M and Crema L. Design and modeling of a hybrid reversible solid oxide fuel cell–organic Rankine cycle. Energy Procedia, 129(2017)331-338.

[35] Ghaffarpour Z, Mahmoudi M, Mosaffa AH and Farshi LG. Thermoeconomic assessment of a novel integrated biomass based power generation system including gas turbine cycle, solid oxide fuel cell and Rankine cycle. Energy conversion and management, 161(2018)1-12.

[36] Owebor K, Oko C.O.C., Diemuodeke E.O. and Ogorure OJ. Thermo-environmental and economic analysis of an integrated municipal waste-to-energy solid oxide fuel cell, gas-, steam-, organic fluid-and absorption refrigeration cycle thermal power plants. Applied Energy, 239(2019)1385-1401.

[37] Ibrahim TK, Rahman MM and Abdalla AN. Gas turbine configuration for improving the performance of combined cycle power plant. Procedia Engineering, 15(2011)4216-4223.

[38] Luo XJ and Fong KF. Development of 2D dynamic model for hydrogen-fed and methane-fed solid oxide fuel cells. Journal of Power Sources, 328(2016)91-104.

[39] Luo XJ and Fong KF. Investigation on control optimization of solid oxide fuel cell-driven combined cooling and power system. Energy Procedia, (2017)1883-1888

[40] Luo XJ. Development of Dynamic Model and Control Strategy of Combined Cooling, Heating and Power System Primed with Solid Oxide Fuel Cell-Gas Turbine for Building Application. PhD Thesis. City University of Hong Kong. 2018.

[41] Zhang N and Cai RX. Analytical solutions and typical characteristics of part-load performances of single shaft gas turbine and its cogeneration. Energy Conversion and Management, 43 (2002) 1323-1337.

[42] Ahmadi MH, Hosseinzade H, Sayyaadi H, Mohammadi AH and Kimiaghalam F. Application of the multi-objective optimization method for designing a powered Stirling heat engine: design with maximized power, thermal efficiency and minimized pressure loss. Renewable Energy, 60(2013)313-322.

[43] Lai NA, Wendland M and Fischer J. Working fluids for high-temperature organic Rankine cycles. Energy, 36(2011)199-211.

[44] J.P. Holman. Heat Transfer (Sixth edition). McGraw-Hill Book Company. (1997).

[45] Cinti G, Bidini G and Hemmes K. Comparison of the solid oxide fuel cell system for micro CHP using natural gas with a system using a mixture of natural gas and hydrogen. Applied Energy, 238(2019)69-77.

Appendix A

A.1 Pre-heater

Pre-heater is a type of heat exchanger and can be regarded as a single control volume. In the pre-heaters, inlet air, fuel and water flow were regarded as cold fluids, while the exhaust gas mixture from the burner was treated as the hot fluid. The counter-flow heat exchanger was adopted, and the pinch temperature is 10 [44]. Based on energy balance, thermal energy increase rate of cold fluid $Q_{PH,c}$ equaled to the energy decrease rate of hot fluid $Q_{PH,h}$:

$$Q_{PH,cf} = Q_{PH,hf} \tag{A1}$$

$$\varepsilon_{PH} = Q_{PH,cf}/Q_{PH,max} \tag{A2}$$

where,

$Q_{PH,cf}$: thermal energy increase rate of cold fluid ($kJ \cdot h^{-1}$)

$Q_{PH,hf}$: thermal energy decrease rate of hot fluid ($kJ \cdot h^{-1}$)

ε_{PH}: the effectiveness of the pre-heater

$Q_{PH,max}$: the maximum heat transfer rate of the pre-heater ($kJ \cdot h^{-1}$)

A.2 Reformer

The reformer is a small packed bed reactor where endothermic methane steam reforming (MSR) reaction and water gas shift (WGS) reaction occur, so that an amount of the methane is converted into hydrogen. Thermal equilibrium of the reformer is obtained by controlling the recovered heat from the exhaust gas. In the modelling of the reformer unit, chemical equilibrium of all reformer reactions was assumed at the outlet temperature [45]. The reformer was regarded as a single control volume and the energy consumption rate of the reformer was calculated as:

$$Q_{re} = (r_{re,MSR}\, q_{MSR} + r_{re,WGS}\, q_{WGS})/\eta_{re} \quad \text{(A3)}$$

where,

q_{MSR}: molar heat consumption of MSR reaction ($kJ \cdot kmol^{-1}$)

q_{WGS}: molar heat production of WGS reaction ($kJ \cdot kmol^{-1}$)

η_{re}: efficiency of the reformer

$r_{re,MSR}$: rate of MSR reaction in the reformer ($kmol \cdot h^{-1}$)

$r_{re,WGS}$: rate of WGS reaction in the reformer ($kmol \cdot h^{-1}$)

Q_{re}: heat consumption rate of the reformer ($kJ \cdot h^{-1}$)

A.3 Burner

The outlet gas mixture from the SOFC stack consisted of CH_4, CO, H_2, H_2O, CO_2, O_2 and N_2. Since there was sufficient air, CH_4, CO and H_2 from the SOFC stack could be fully oxidized in the burner. Based on energy balance, the total enthalpy of the outlet gas mixture equaled to the sum of enthalpy of the inlet gas mixture and lower heating value (LHV) of the combusted gases:

$$h_{bu,in} + (n_{bu,CH4,in}\, LHV_{CH4} + n_{bu,CO,in}\, LHV_{CO} + n_{bu,H2,in}\, LHV_{H2})\, \eta_{bu} = h_{bu,out} \quad \text{(A4)}$$

where,

$h_{bu,in}$: total specific enthalpy of inlet gas mixture to the burner ($kJ \cdot kg^{-1}$)

$h_{bu,out}$: total specific enthalpy of outlet gas mixture from the burner ($kJ \cdot kg^{-1}$)

η_{bu}: efficiency of the burner (%)

A.4 Absorption chiller and compression chiller

The cooling capacity of AbC in the SOFC-primed CCP reference system $C_{AbC,S0}$ was determined by the recoverable thermal energy $Q_{AbC,S0}$ (kJ·h^{-1}) at Point 15 and the coefficient of performance *COP* of the AbC COP_{AbC}:

$$C_{AbC,S0} = COP_{AbC}\, Q_{AbC,S0} \tag{A5}$$

The cooling capacity of the AbC in the SOFC-GT-primed CCP system $C_{AbC,S1}$ was determined by the recoverable thermal energy $Q_{AbC,S1}$ (kJ·h^{-1}) at Point 17:

$$C_{AbC,S1} = COP_{AbC}\, Q_{AbC,S1} \tag{A6}$$

The cooling capacity of the AbC in the SOFC-SE-primed CCP system $C_{AbC,S2}$ was determined by the recoverable thermal energy $Q_{AbC,S2}$ (kJ·h^{-1}) at Point 16 and the thermal energy provided by the cooler $Q_{SE,co}$:

$$C_{AbC,S2} = COP_{AbC}\, (Q_{AbC,S2} + Q_{SE,co}) \tag{A7}$$

For A-type SOFC-ORC-primed CCP system, both the thermal energy of condenser Q_{con} and the recoverable heat at Point 16 $Q_{AbC,S3}$ could be used to drive AbC. The cooling capacity of AbC $C_{AbC,S3,A}$ was calculated as:

$$C_{AbC,S3,A} = COP_{AbC}\, (Q_{AbC,S3} + Q_{con}) \tag{A8}$$

In B-type SOFC-ORC-primed CCP system, the condenser temperature was set at 300 K. Thus only the thermal energy recovered from Point 16 was supplied to AbC. The cooling capacity of AbC in this type of system $C_{AbC,S3,B}$ was determined as:

$$C_{AbC,S3,B} = COP_{AbC}\, Q_{AbC,S3} \quad \text{(A9)}$$

The cooling capacity of CoC was determined its power consumption P_{CoC} (kJ·h^{-1}) and the *COP* of CoC, COP_{CoC}:

$$C_{CoC} = COP_{CoC}\, P_{CoC} \quad \text{(A10)}$$

Appendix B

B.1 SOFC-primed CCP reference system

In Table B.1, the thermodynamic properties of the SOFC-primed CCP reference system is based on current density J = 6000 A/m^2 and fuel inlet temperature $T_{f,in}$ = 1123 K at SOFC stack. Air, methane and water is heated up from 297 K (i.e. room temperature) to 1123 K before being fed to the SOFC stack. Through the SOFC stack, there is fluid temperature increase of 128 K (= 1251 K – 1123 K for Points 9 and 8). Then through the burner, there is increase of 323 K (= 1574 K – 1251 K for Points 10 and 9). After exchanging heat with the reformer and the three pre-heaters, the temperature of the exhaust gas decreased to 634 K (Point 12, 13 or 14), which was used to provide thermal energy for the AbC. The leaving temperature of exhaust gas from the AbC is designed at 373 K (Point 15).

Table B.1. Thermodynamic properties of each fluid flow of SOFC-primed CCP reference system.

State point	T (K)	P (bar)	n (mol·s^{-1})	Molar fraction (%)						
				CH_4	O_2	N_2	H_2	CO	CO_2	H_2O
1	297	1.013	142		21	79				
2	1123	1.013	142		21	79				
3	297	1.013	6	100						
4	297	1.013	15							100
5	297	1.013	15							100
6	1123	1.013	6	100						
7	1123	1.013	15							100
8	1123	1.013	36	17.1			26.3	2.9	4.4	49.3
9	1251	1.013	175	0.0329	8.53	64.08	3.41	0.90	4.06	20.49
10	1574	1.013	172		7.1	65.0			5.1	22.9
11	1493	1.013	172		7.1	65.0			5.1	22.9
12	634	1.013	149		7.1	65.0			5.1	22.9
13	634	1.013	6.7		7.1	65.0			5.1	22.9
14	634	1.013	16.3		7.1	65.0			5.1	22.9
15	634	1.013	172		7.1	65.0			5.1	22.9
16	373	1.013	172		7.1	65.0			5.1	22.9

B.2 SOFC-GT-primed CCP system

In Table B.2, the thermodynamic properties of the SOFC-GT-primed CCP system are based on current density J = 6000 A/m^2, fuel inlet temperature $T_{f,in}$ = 1123 K and compression ratio π_{GT} = 4. Since the inlet temperature of air in PH1 (476 K at Point 2) is higher than that of PH2 and PH3 (297K at Points 4 and 5), the mass flow rate of exhaust gas through PH1 is designed such that it is sufficient to heat up the air flow to $T_{f,in}$. Since the operating pressure of the SOFC stack in the SOFC-GT-primed CCP system is higher than that in the SOFC-primed CCP reference system, the outlet gas mixture of the SOFC stack (Point 10) and the burner (Point 11) is lower. In the GT, thermal energy of the exhaust gas is converted into electrical power thus its temperature decreases to 1228 K (Point 12). After providing thermal energy for the reformer and the pre-heaters, the temperature of exhaust gas becomes 412 K (Point 14, 15 or 16). The leaving temperature of exhaust gas from the AbC is designed at 373 K (Point 17), same as that set in the SOFC-primed CCP reference system.

Table B.2. Thermodynamic properties of each fluid flow of SOFC-GT-primed CCP system.

State point	T (K)	P (bar)	n (mol·s^{-1})	Molar fraction (%)						
				CH_4	O_2	N_2	H_2	CO	CO_2	H_2O
1	297	1.013	142		21	79				
2	476	4.052	142		21	79				
3	297	1.013	6	100						
4	297	1.013	15							100
5	297	1.013	15							100
6	1123	4.052	142		21	79				
7	1123	1.013	6	100						
8	1123	1.013	15							100
9	1123	1.013	36	17.1			26.3	2.9	4.4	49.3
10	1221	4.052	175	0.0329	8.53	64.08	3.41	0.90	4.06	20.49
11	1540	4.052	172		7.1	65.0			5.1	22.9
12	1228	1.013	172		7.1	65.0			5.1	22.9
13	1144	1.013	172		7.1	65.0			5.1	22.9
14	412	1.013	149		7.1	65.0			5.1	22.9
15	412	1.013	6.7		7.1	65.0			5.1	22.9
16	412	1.013	16.3		7.1	65.0			5.1	22.9
17	412	1.013	172		7.1	65.0			5.1	22.9
18	373	1.013	172		7.1	65.0			5.1	22.9

B.3 SOFC-SE-primed CCP system

In Table B.3, the thermodynamic properties of the SOFC-SE-primed CCP system is based on J = 6000 A/m^2, $T_{f,in}$ = 1123 K and using α-SE. The thermodynamic properties of Points 1-10 are the same as those in the SOFC-primed CCP reference system. After combusted in the burner, the thermal energy of the hot exhaust gas mixture is recovered to provide thermal energy for the SE. The temperature of outlet gas from the SE hot side (Point 11) is designed at 1343 K, so that there is sufficient thermal energy for the reformer and the pre-heaters. The temperature of gas mixture before entering AbC was 400 K, which is lower than those in SOFC-primed CCP reference system and SOFC-GT-primed CCP system. Therefore, the cooling capacity of the AbC will be lower. AbC is also used as the heat sink for the SE. Hot water is heated from 360 K (Point 18) to 365 K (Point 19) through the SE, which can be used to energize the AbC.

Table B.3. Thermodynamic properties of each fluid flow of SOFC-SE-primed CCP system.

State point	T (K)	P (bar)	n (mol·s^{-1})	Molar fraction (%)						
				CH_4	O_2	N_2	H_2	CO	CO_2	H_2O
1	297	1.013	142		21	79				
2	1123	1.013	142		21	79				
3	297	1.013	6	100						
4	1123	1.013	6							100
5	297	1.013	15							100
6	297	1.013	15		21	79				
7	1123	1.013	15	100						
8	1123	1.013	36	17.1			26.3	2.9	4.4	49.3
9	1251	1.013	175	0.0329	8.53	64.08	3.41	0.90	4.06	20.49
10	1574	1.013	172		7.1	65.0			5.1	22.9
11	1343	1.013	172		7.1	65.0			5.1	22.9
12	1259	1.013	172		7.1	65.0			5.1	22.9
13	400	1.013	149		7.1	65.0			5.1	22.9
14	400	1.013	6.7		7.1	65.0			5.1	22.9
15	400	1.013	16.3		7.1	65.0			5.1	22.9
16	400	1.013	172		7.1	65.0			5.1	22.9
17	373	1.013	172		7.1	65.0			5.1	22.9
18	360	1.013	0.34							100
19	365	1.013	0.34							100

B.4 SOFC-ORC-primed CCP system

In Table B.4, the thermodynamic properties of the B-type SOFC-ORC-primed CCP system is based on $T_{f,in}$ = 1123 K and using o-Xylene as the working fluid. Since the temperature requirement of ORC evaporator is around 600 K, the exhaust gas is delivered to the reformer and the three pre-heaters before going through the evaporator. At the design condition, the outlet gas mixture from the evaporator is 580 K (Point 15), which is lower than that in the SOFC-primed CCP reference system, but higher than those in SOFC-GT- and SOFC-SE-primed CCP systems. Through utilizing the thermal energy of the condenser, hot water is heated from 360 K (Point 22) to 365 K (Point 23). Such hot water is used to energize the AbC.

Table B.4. Thermodynamic properties of each stream of the SOFC-ORC-primed CCP system.

State point	T (K)	P (bar)	n ($mol \cdot s^{-1}$)	Molar fraction (%)						
				CH_4	O_2	N_2	H_2	CO	CO_2	H_2O
1	297	1.013	142		21	79				
2	1123	1.013	142		21	79				
3	297	1.013	6	100						
4	1123	1.013	6							100
5	297	1.013	15							100
6	297	1.013	15		21	79				
7	1123	1.013	15	100						
8	1123	1.013	36	17.1			26.3	2.9	4.4	49.3
9	1251	1.013	175	0.0329	8.53	64.08	3.41	0.90	4.06	20.49
10	1574	1.013	172		7.1	65.0			5.1	22.9
11	1493	1.013	172		7.1	65.0			5.1	22.9
12	634	1.013	172		7.1	65.0			5.1	22.9
13	634	1.013	149		7.1	65.0			5.1	22.9
14	634	1.013	6.7		7.1	65.0			5.1	22.9
15	634	1.013	16.3		7.1	65.0			5.1	22.9
16	580	1.013	172		7.1	65.0			5.1	22.9
17	373	1.013	172		7.1	65.0			5.1	22.9
18	630	30	5.68							
19	444	0.01	5.68							
20	400	0.01	5.68							
21	400	30	5.68							
22	360	0.10	0.10							100
23	365	0.10	0.10							100